VARIABLE-DENSITY OSCILLATORY FLOW AND HEAT TRANSFER IN 2D MODELS OF A STIRLING MICROREFRIGERATOR

By

GUOBAO GUO

A DISSERTATION PRESENTED TO THE GRADUATE SCHOOL
OF THE UNIVERSITY OF FLORIDA IN PARTIAL FULFILMENT
OF THE REQUIREMENTS FOR THE DEGREE OF
DOCTOR OF PHILOSOPHY

UNIVERSITY OF FLORIDA

1996

ACKNOWLEDGMENTS

I would like to thank my supervisor, Professor Ulrich H. Kurzweg, for his guidance, constant encouragement and patience. I have greatly benefited not only from his teaching in engineering but also from his integrity, which has had a positive influence on my life. I sincerely thank Dr. Chen-Chi Hsu for giving me the opportunity to join the graduate program here and for teaching me many of the fundamental, yet important, aspects of CFD during my first phase of graduate course work. Likewise, I am very grateful to Dr. Wei Shyy for our discussions and his fruitful suggestions in my work. I also express my appreciation to my other supervisory committee members, Dr. David M. Mikolaitis and Dr. Kermit N. Sigmon, for their interest and suggestions.

My special thanks go to my fellow graduate students of the department here for their help and companionship. I especially thank Dr. Ming-Hsiung Chen for his warm friendship, help and encouragement over the years.

I am thankful to the Department of Aerospace Engineering, Mechanics and Engineering Science for providing financial assistance. I extend my special thanks to Dr. Michael A. DeLorenzo of the Dairy and Poultry Science Department and Dr. Ranganatha Narayanan of the Chemical Engineering Department for offering me part-time jobs during my study, which exposed me to some other interesting engineering and management problems. They have certainly enriched my education.

I am truly grateful to my wife Ying for her love, patience and encouragement during this work, which were more than I could ever have requested.

The Pittsburgh Supercomputing Center supported this work through the allocation of 183 Service Units on the Cray C90 supercomputer for three and half years, and is acknowledged here.

TABLE OF CONTENTS

page

ACKNOWLEDGMENTS ii

LIST OF TABLES vi

LIST OF FIGURES vii

ABSTRACT ix

CHAPTERS

1 INTRODUCTION 1

1.1 Background of Stirling Refrigerators 1
1.2 Literature Review 13
1.3 2D Computational Models and Scope of the Present Work 17

2 GOVERNING EQUATIONS AND PRESSURE-SPLITTING TECHNIQUE 22

2.1 Governing Equations 22
2.2 Separation of Hydrodynamic and Thermodynamic Pressures 25
2.3 Boundary Conditions 28
2.4 Nondimensionalization of Governing Equations and Boundary Conditions 30
2.5 General Form of the Governing Equations 34
2.6 Dimensional Analysis 35

3 NUMERICAL TECHNIQUES AND CODE VALIDATION 37

3.1 Numerical Grid Generation 37
3.2 Discretization of the Governing Equations 40
3.3 Solution Procedures 49
3.4 Initial and Slow-Start Boundary Condations 54
3.5 Code Validation 57

4 RESULTS AND DISCUSSION 65

4.1 Velocity and Thermodynamic Fields for a Typical Case 68
4.2 Model Comparison 82
4.3 Comparison of Using Helium and Air 85
4.4 Phase Angle Effect 86
4.5 Impact of Varying Refrigeration Temperatures on Performances ... 87
4.6 Changing Channel Length 89
4.7 Effects of Changing the Ratio of Chamber Width to Channel Width 90
4.8 Discussion on Regeneration 91

5 CONCLUDING REMARKS 95

REFERENCES 98

BIOGRAPHICAL SKETCH 104

LIST OF TABLES

Table		page
Table 2.1	Terms in the governing equation (2.34)	35
Table 4.1	List of the cases investigated	66
Table 4.2	Comparison of Models A1 and A2	83
Table 4.3	Comparison of Models A2 and B2	84
Table 4.4	Comparison of helium and air	85
Table 4.5	Comparison of cases with different channel lengths	89

LIST OF FIGURES

Figure		page
Fig. 1.1	Stirling cycle and a three-component Stirling refrigerator configuration	2
Fig. 1.2	Schematic of a five-component Stirling refrigerator	5
Fig. 1.3	Single-channel models. (a) Model A1; (b) Model A2	18
Fig. 1.4	Multichannel models. (a) Model B1; (b) Model B2	19
Fig. 2.1	Illustrative 1D discretization	26
Fig. 3.1	Two typical grids. (a) $\omega t = \pi/4$; (b) $\omega t = \pi$	39
Fig. 3.2	1D grids	39
Fig. 3.3	Control volumes for scalar quantities	42
Fig. 3.4	Staggered u and v control volumes	42
Fig. 3.5	Schematic of a general cell for ϕ at point P	43
Fig. 3.6	A south boundary cell with Dirichlet boundary condition	48
Fig. 3.7	A south boundary cell with Neumann boundary condition	48
Fig. 3.8	Solution procedures for variable-density time-periodic flow and heat transfer problems	55
Fig. 3.9	A piston-cylinder set-up	58
Fig. 3.10	Computed hydrodynamic pressure distributions along the x axis for the piston-cylinder set-up	58
Fig. 3.11	Thermodynamic pressure in the third cycle for the piston-	

cylinder set-up 61

Fig. 3.12 Temperature distributions along the x axis for the piston-cylinder set-up 61

Fig. 3.13 P-V diagram of the second test case 63

Fig. 4.1 Transient processes of pressures.
(a) Thermodynamic pressure; (b) Pressure drop between pistons. 69

Fig. 4.2 Convergence history to time-periodic state 71

Fig. 4.3 Velocity fields of Case 1
(a) $\omega t=0$; (b) $\omega t=\pi/2$; 72
(c) $\omega t=\pi$; (d) $\omega t=3\pi/2$. 73

Fig. 4.4 Hydrodynamic pressure contours of Case 1
(a) $\omega t=0$; (b) $\omega t=\pi/2$; 74
(c) $\omega t=\pi$; (d) $\omega t=3\pi/2$. 75

Fig. 4.5 Temperature contours of Case 1
(a) $\omega t=0$; (b) $\omega t=\pi/2$; 77
(c) $\omega t=\pi$; (d) $\omega t=3\pi/2$. 78

Fig. 4.6 Density contours of Case 1
(a) $\omega t=0$; (b) $\omega t=\pi/2$; 79
(c) $\omega t=\pi$; (d) $\omega t=3\pi/2$. 80

Fig. 4.7 P-V diagram of Case 1 81

Fig. 4.8 Phase angle effects 87

Fig. 4.9 Refrigeration temperature effects 88

Fig. 4.10 Effects of changing the ratio of chamber width to channel width 91

Fig. 4.11 Temperature distributions along x axis for two different β's
(a) $\beta = 0.0298$; (b) $\beta = 0.298$ 94

Abstract of Dissertation Presented to the Graduate School
of the University of Florida in Partial Fulfilment of the
Requirements of the Degree of Doctor of Philosophy

VARIABLE-DENSITY OSCILLATORY FLOW AND HEAT TRANSFER
IN 2D MODELS OF A STIRLING MICROREFRIGERATOR

By

Guobao Guo

May 1996

Chairperson: Dr. Ulrich H. Kurzweg
Major Department: Aerospace Engineering, Mechanics and Engineering Science

Two-dimensional models of three-component Stirling microrefrigerators are examined. The models consist of heater and cooler ended with pistons oscillating out of phase and connected by narrow channels with a linear wall-temperature distribution, simulating the regenerator. Navier-Stokes equations governing the variable-density, oscillatory flow and heat transfer within two-dimensional domains with moving boundaries are numerically solved by using the SIMPLE algorithm incorporated into a moving grid technique and a pressure-splitting technique that is newly developed in this study. Such a solution methodology is accurate and efficient for the complex flow and heat transfer problems in Stirling-type devices. The pressure-splitting technique separates the hydrodynamic and thermodynamic pressures, which are different by orders of magnitude for gaseous flows with heat transfer like those in reciprocating machines.

Separation of the pressures increases the computing accuracy and efficiency substantially (with saving on memory by 50% and on CPU time by 30%), and the technique can be easily incorporated to any pressure-based numerical algorithms. The model's cooling performance is sensitive to a dimensionless parameter that is the product of Prandtl number, Womersley number squared, and two dimensionless geometric parameters. This parameter should be kept small enough for the regenerator to function well. As the refrigeration temperature decreases, the cooling capacity decreases linearly, but the power input increases linearly, and consequently the performance degrades. It is found that for a set of given operation conditions, there exists a lowest temperature below which no cooling becomes possible. This is caused by the increasing cooling loss through the channel as the refrigeration temperature decreases. Lengthening the channels decreases such loss, but meanwhile increases the dead space, which in turn reduces the cooling made by the expansion. The net effect depends on these two competing factors under specific conditions. The phase angle affects the cooling capacity and efficiency, and the optimum phase angle for either cooling capacity or efficiency is near 90°. For the multichannel model, the ratio of the chamber width to the channel width also affects the cooling performance, and the optimum ratio depends on specific operation conditions.

CHAPTER 1
INTRODUCTION

1.1 Background of Stirling Refrigerators

1.1.1 The Stirling Principle

With the ban on the production of chlorofluorocarbon (CFC) refrigerants in the U.S. after January 1, 1996 (and eventually the ban on the use of them worldwide), alternative cooling devices such as Stirling refrigerators, pulse tube refrigerators and thermoacoustic refrigerators have received more and more attention (Chase 1995). The Stirling refrigerator is named after Scottish clergyman Robert Stirling who invented the Stirling engine in 1816. A Stirling-type device uses a common gas (not ozone-depleting CFCs), usually air or helium, as the working medium and works in a closed cycle. By compressing and expanding the gas in two separated chambers at different temperatures, either refrigeration is obtained by doing work on the gas (as in a refrigerator), or mechanical power is produced by consuming heat (as in an engine). Figure 1.1 illustrates the working principle of a Stirling cooling device. The device consists of three basic heat-exchanging components: the cold chamber, the hot chamber and the regenerator, so it is called a three-component configuration. As shown in the figure, the chambers are connected by a regenerator. In each chamber, there is a piston oscillating out of phase with the piston in the other chamber. The regenerator is made of metallic

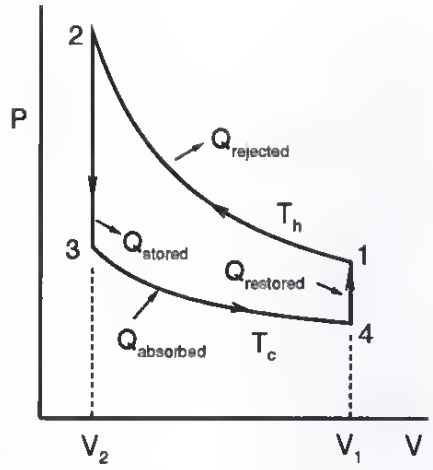

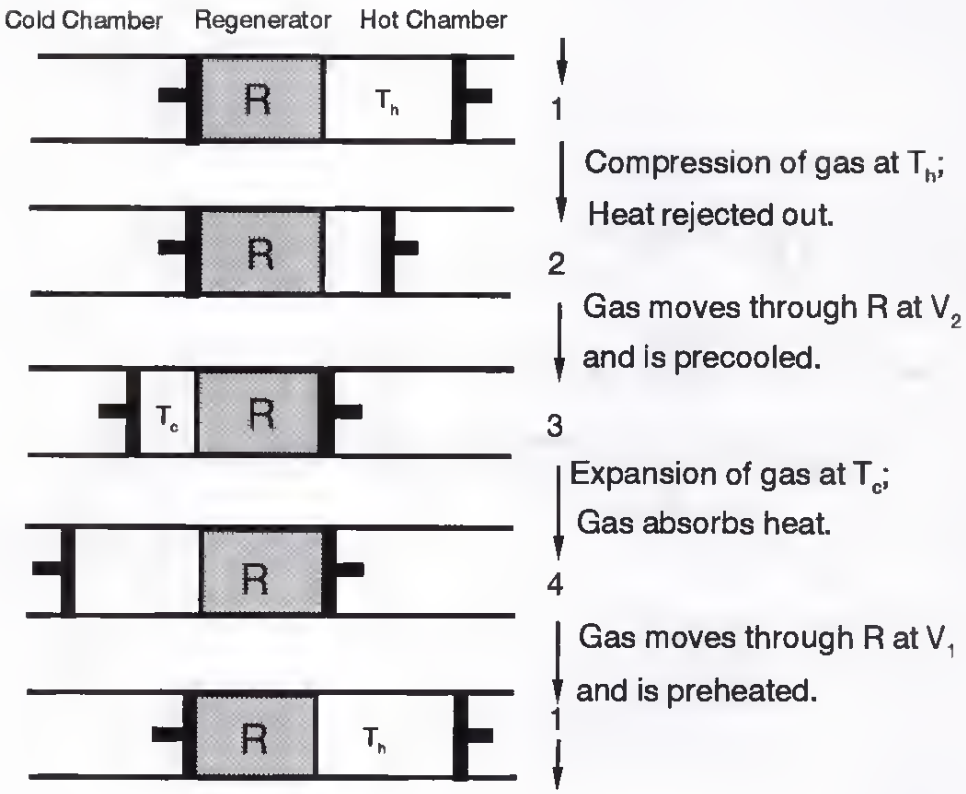

Fig. 1.1 Stirling cycle and a three-component Stirling refrigerator configuration

porous materials, so it has an extremely high thermal capacity compared with the working gas and meanwhile has excellent thermal contact with the gas in it. It functions as a heat sponge, periodically absorbing and releasing heat from and to the gas flowing through it. The Stirling cycle consists of four idealized processes indicated in Fig. 1.1.

Process 1-2--Isothermal Compression:

All the gas is located in the hot chamber at temperature T_h and the right piston compresses the gas. As a result, heat is rejected from the gas through the chamber wall.

Process 2-3--Constant Volume Precooling:

The two pistons move in unison to keep the total volume constant and to move the hot gas from the hot chamber to the cold chamber through the regenerator. During this process, heat is stored in the regenerator and the gas is precooled.

Process 3-4--Isothermal Expansion:

All the gas is in the cold chamber at temperature T_c and the left piston expands. Owing to the expansion, heat is absorbed by the gas through the chamber wall. Thus, refrigeration is achieved.

Process 4-1--Constant Volume Preheating:

The pistons move in unison so the total volume is constant and the cold gas is moved from the cold chamber to the hot chamber through the regenerator. The previously stored heat in the regenerator is now released back to the cold gas. Then the closed system is ready for the next cycle.

The above discussion is based on highly idealized conditions under which the piston motions are discontinuous as indicated in Fig. 1.1, and all the gas is in the hot

chamber during the compression and all is in the cold chamber during expansion. The seidealized conditions also imply perfect heat transfer and infinite heat capacity of the regenerator so that gas temperature in either end chamber is maintained constant and the compression or expansion is isothermal, and the amount of heat absorbed by the regenerator is exactly the same as that restored. It is not so in reality. First, since the discontinuous piston motions are mechanically difficult to implement, the pistons in a real Stirling cooling device usually oscillate sinusoidally such that the hot-chamber volume variation leads the cold-chamber volume variation by a phase angle of about 90°. Second, it is not possible for all the gas to be in either end chamber for compression or expansion because there is always some gas in the regenerator or in other pockets (the volume that can not be swept by pistons is called dead space). And finally, both the thermal capacity of the regenerator and the rate of heat transfer between the gas and the three exchangers are finite. Therefore, the gas in the chambers does not exactly have the wall temperature and the regenerator may not function perfectly either. As a result of these complicating factors, the thermodynamic cycle is not precisely composed of two isothermal and two equal-volume processes, and the actual P-V diagram will be somewhat different from the one shown in Fig. 1.1 (Chapter 4 will show a realistic P-V diagram).

In the three-component configuration, the expansion or compression takes place in the big end chambers, so there may not be enough time and area for heat exchange between the gas and the chamber walls. For better performance, usually the compression and expansion chambers are separated from the heating area (heater) and the cooling area

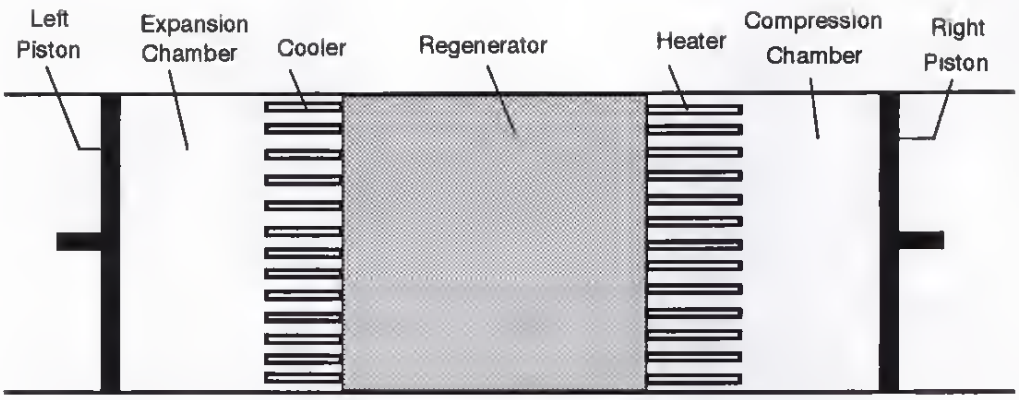

Fig. 1.2 Schematic of a five-component Stirling refrigerator

(cooler), respectively. The heater or cooler is made up of many metal tubes of small diameters such that the heat transfer is adequate. Figure 1.2 demonstrates a five-component configuration.

1.1.2 Brief History of Stirling Machine Development and Applications

Details on the development history of Stirling-type devices can be found in books by Walker (1973), Reader and Hooper (1983), West (1986) and Organ (1992). Since Stirling's invention almost two centuries ago, many different Stirling devices have been developed and found their various potential and actual applications: automotive engines, small electric generators, underwater power units, solar thermal conversion, space power, artificial heart power, heat pumping, cryogenic cooling engines (cryocoolers), near-ambient-temperature refrigerating machines (refrigerators). The early and primary developments focused only on machines providing mechanical driving power (i.e., prime

movers). After the middle of the nineteenth century, because of the inventions of the internal combustion engine and electric motor, the Stirling prime movers gradually lost their commercial market to these new inventions. However, the appealing characteristics of the Stirling engine still attracted engineers to continue research and development. When working as a prime mover, a Stirling engine can use essentially all kinds of heat sources: solid, liquid or gaseous fossil fuel combustion, solar heat, nuclear heat, etc. The combustion with a Stirling engine is external and the process can be easily controlled, producing a lower air pollution level than an internal combustion engine. The Stirling engine does not require any valves to control the flow or pressure, and the combustion (if needed) does not result in periodic explosions. So the engine is very quiet and the machine vibration is very small in comparison with other engines. When working as a refrigerator a Stirling refrigerator uses no CFCs, so it is environmentally safe.

One of the leading institutions for the Stirling devices is the Philips Research Laboratories in Eindhoven, Holland. Back to the late 1930s, Philips developed portable Stirling electric generators for radio sets. Later they studied and applied new technologies to the then existing Stirling engines. By the mid-1940s, they had increased the Stirling engine's power per unit weight by a factor of 50, increased its size per unit power by a factor of 125 and improved its efficiency by a factor of 15 (Reader and Hooper 1983). It is Philips who brought the Stirling engine into its modern era.

From the late 1950s, Philips along with several European and American companies (including Ford and GM) began to develop Stirling automotive engines.

When the oil crisis hit the world in the 1970s, the interest in such engines increased suddenly because of the wide variety of energy (heat) sources that could be used by Stirling engines. In 1978, sponsored by the U.S. Department of Energy, several U.S. companies including the AM General Corporation, Mechanical Technology Inc. (MTI) and the United Stirling carried out intensive researches in hopes of replacing the internal combustion diesel and gasoline engines in automobiles. The main difficulty with Stirling automotive engines becoming commercialized is that they cannot compete with existing diesel and gasoline engines in manufacture and maintenance costs because the latter have already been well developed and are under continuous improvement. As a result, all Stirling automotive programs stopped about a decade ago.

One of the active areas in the Stirling research and development is the artificial heart. Since the 1960s the U.S. National Institutes of Health and some companies (e.g., Stirling Technology Company) have been developing totally implantable artificial heart devices (West 1986, White 1985). Its merits of quietness, very small vibration and high reliability make the Stirling engine the best power provider for this purpose. A small Stirling engine in such devices uses radioisotopes as the heat source for a long and continuous life.

Since the 1960s the Stirling engine has been identified as the key to the future space energy conversion systems by NASA Lewis Research Center (LeRC) (Shaltens and Schreiber 1989). The heat sources for the systems can be nuclear reactor heat, radioisotopic heat or solar heat. Stirling systems have the potential of meeting space power's requirements: high power capacity, high thermal efficiency, high reliability, low

vibration and very long life. NASA initiated the free-piston Stirling space power program in the mid-1980s, and a research engine was built by MTI under contract with NASA (Tew 1988). Some main design goals are: output electric power 12.5 kW, thermal efficiency 25%, life 60,000 hours (seven years), hot-end temperature 1050 K, cold-end temperature 525 K, frequency 70 Hz and mean pressure 150 atms. Initial test results with the originally built engine indicated that the engine performance did not reach the design goal (Tew 1988). NASA LeRC, MTI and several other U.S. companies have done intense experimental and analytical work in the past several years (Cairelli et al. 1989-1991 & 1993, Dochat 1990, Jones 1990, Dochat and Dhar 1991, Thieme and Swec 1992, Wong et al. 1992), and some significant improvements on the engine have been made and novel component technologies have been obtained.

The commercialization of Stirling solar energy conversion systems has been pursued for almost two decades in several countries, e.g., Germany (Keck et al. 1990), Japan (Isshiki et al. 1991), Russian (Loktinonov 1991), Sweden (Diver et al. 1990) and the U.S. (Andraka et al. 1994). In such systems the solar heat is collected by a parabolic dish and used as the heat source of a Stirling engine, then the engine can drive a water pump for irrigation or drive an electrical generator for electricity supply. The Stirling solar system is more efficient than conversion systems using photovoltaic cells. In the early solar Stirling engines, collected solar rays were aimed directly at the engine heater tubes. This produced very hot spots in the tubes and so the temperature distribution there was not uniform, resulting in a too restrictive requirement on materials and thus limiting the engine life and performance. To solve this problem, a liquid-metal reflux

receiver is used to transport the collected solar energy to the heater tubes. In the reflux receiver, a liquid metal (usually sodium or sodium-potassium alloy NaK-78) evaporates at the solar absorber due to the very high temperature there, and then condenses at the engine heater tubes. The latent heat released by the condensing vapour is utilized to heat the tubes. Most of the current technology advances are made in the U.S., primarily due to the Department of Energy's Solar Thermal Program and the studies made by some private companies.

The most successful commercial application of the Stirling engine is cooling. Seventeen years after Stirling's invention, John Herschel in 1834 realized that the Stirling machine could also work as a refrigerator, and the first Stirling refrigerator was built by Gorrie in 1845 (Köhler 1960). A review on the applications of Stirling refrigerators was given by Walker et al. (1988). In 1954 Philips first commercialized a Stirling cryocooler with a cooling capacity of 1 kW at 80 K for air liquefaction. Since then Stirling refrigerators have been commercially developed for various applications with a cooling capacity from a few milliwatts to several kilowatts and with refrigeration temperatures from as low as a few degrees Kelvin to near ambient. At very low temperatures, usually below 160 K, the efficiency of a Stirling refrigerator is much higher than all other cooling devices such as the ones using the Joule-Thomson effect, or the ones using the evaporation of a liquid (i.e., the commonly used refrigerators). So Stirling refrigerators have dominated the world market of gas liquefiers for half a century. Liquified gases are mainly used for cryogenic experiments, in which the temperature is usually in the cryogenic range, namely below 120 K. With the findings of more and more high-

temperature superconductors and their increasing applications in electronics, the current need for Stirling cryocoolers is more demanding than ever.

Beside the large cryocoolers for gas liquefaction, small and miniature Stirling cryocoolers have also been widely used to cool some special small sensors and electronic components that need cryogenic cooling for higher resolution and sensitivity. These include infrared detectors, X-ray and γ-ray solid state-detectors, etc. Increasing numbers of such detectors are carried by airplanes, space shuttles, space stations, satellites and deep space probes for civilian and military purposes (e.g., Earth observation, atmospheric science, astronomy and space surveillance). Since the 1960s, many efforts have been made in the U.S. to develop spaceborne cryogenic systems (Sherman 1982). The required cooling power for the systems is usually between a few milliwatts and tens of watts at temperatures below 80 K. Due to the restriction on the size and weight of the loads in space missions (especially the long-term ones), it is not feasible to carry a large amount of solid or liquid cryogens with spacecraft. Therefore miniature mechanical cryocoolers (of the Stirling, Joule-Thompson absorption, pulse tube, acoustic, turbo Brayton and magnetic types) have been pursued because of their small size and lightweight, mechanical quietness, and expected very long life without maintenance. As reported by Chan et al. (1990), of all the eight known space flights (between 1970 and 1989) using mechanical cryocoolers, Stirling cryocoolers were flown six times. The lead of the Stirling cryocooler over others is attributed to the mature technologies for the large-size Stirling cryocoolers as mentioned before and to its higher efficiency than others in the temperature range of interest.

In search of alternatives to the existing CFC-containing vapour-compression refrigerators exclusively used at near ambient temperatures, the Stirling refrigerator has recently been considered as a promising contender (Walker et al. 1992, Berchowitz 1992, Chase 1995). According to Walker et al., at near ambient temperatures, the coefficient of performance of a vapour-compression refrigerator is about 60-70% of the Carnot value, whereas that of the Stirling refrigerator is only about 45% of the Carnot value, and that is why the former has long dominated the refrigeration market at near ambient temperatures. Researchers in many countries are now developing Stirling refrigerators for domestic refrigeration, air conditioning, electronic cooling and so on. In the late 1980s, the NASA Manned Spacecraft Center at Houston, Texas, sponsored a company to build a Stirling refrigerator for manned spacecraft. Air was used as the working fluid in the device, which makes it safe for astronauts in case of refrigerant leakage and simple for gas replenishment since the working gas is just the air in the spacecraft. To replace the existing refrigerator or freezer used in the space shuttle mid-deck for the preservation of experiment samples, primarily blood and urine, NASA's Life Sciences Projects Division at the Johnson Space Center in 1992 also initiated a project to design and develop a Stirling refrigerator (McDonald et al. 1994). The Stirling refrigerator was designed by Sunpower Inc. of Athens, Ohio. This unit used helium as the working fluid, and was lightweight (101 lbs, including the heat pipes), quiet and efficient (heat lift of 90.6 watts at 4°C with a power input of 60 watts, and heat lift of 88.5 watts at -22°C with power input of 70 watts). It was successfully flown on board a space shuttle in February 1994 for three days as a freezer and four days as a refrigerator. Sunpower Inc.

has done pioneer work in developing free-piston Stirling refrigerators for intermediate and near ambient temperatures and in commercializing them (Berchowitz 1992). The company has developed two prototypes of Stirling refrigerators: "Super Fridge" and "Cool Junior." The "Super Fringe" is aimed at replacing the existing domestic vapour-compression refrigerators, and is capable of lifting 250 watts at -26°C with an input of 215 watts. The "Cool Junior" is very small, and so is ideal for cooling electronics, vaccines, etc. It has a cooling capacity of 35 watts at -50°C and 54 watts at -26°C. Work on the development of Stirling refrigerators for domestic applications has also recently been done by Gold-Start Co. of Korea (Kim et al. 1993) and by several Japanese companies and institutions like Toshiba (Otaka et al. 1993, Isshiki et al. 1994). Creare Inc. of Hanover, New Hampshire, has developed a proof-of-principle diaphragm defined Stirling refrigerator for near ambient applications (Shimko et al. 1994). The design innovation in this machine is the application of diaphragms to sweep and seal the compression and expansion volumes. That completely avoids the serious sealing and lubricating problems associated with the pistons in the conventional design.

1.1.3 The Challenges in Analyzing and Simulating Stirling-Type Devices

In reciprocating machines, such as internal combustion engines, Stirling type-devices (prime mover, refrigerators and heat pumps) and pulse tube refrigerators, the flow and heat transfer are time periodic, multidimensional with moving boundaries and with abrupt cross-section changes. Besides, owing to large temporal volumetric oscillations and spatial temperature gradients, density varies significantly in time and in

space, and pressure level also oscillates to a large degree. Moreover, periodic transition to turbulence may also occur for large enough machine dimensions or at high enough operation frequencies, and the time-periodic flow and heat transfer in the porous medium of the regenerator complicates the problem even further. Therefore analysing or numerically simulating such flow and heat transfer remains a challenging task. In the design and analysis of such machines, usually one-dimensional (1D) models are used along with empirical formulas for gas-wall heat transfer coefficients, skin friction coefficients, pressure drops and so on (Reader and Hooper 1983, West 1986). These formulas, however, are correlated only from the experimental data of incompressible (constant-density) steady unidirectional flows; and it has been shown that the formulas and consequently the 1D models are not able to accurately predict the performance of Stirling devices (Geng and Tew 1992, Smith et al. 1992, Cairelli et al. 1993), although they meet such design needs as simplicity and short design cycle.

1.2 Literature Review

A classical thermodynamic analysis method for the Stirling engine was first presented by G. Schmidt in 1861 (Walker 1973). The differences between the Schmidt theory and the highly idealized Stirling cycle are that the Schmidt theory allows for the more realistic sinusoidal piston motions, and that it also takes the dead space into consideration. This theory, however, still retains some of the highly idealized Stirling-cycle assumptions. For example, the gas temperature distribution in each heat exchanger is uniform, therefore the thermodynamic process isothermal; the regeneration is perfect;

pressure drops across engine components are negligible and thus the instantaneous pressure is the same through out the system. Although the method can give closed form solutions based on these assumptions, it is still of very limited use. This is because some assumptions it uses are still far from the real situation, and so the predicated engine characteristic values must be multiplied by a factor of 0.3 to 0.4 in order for them to match those of a real engine.

The Schmidt method was later replaced by newer analytical methods like linear harmonic analysis, which was introduced to the Stirling community after 1960s. West (1984) thoroughly reviewed the linear harmonic analysis method. This method regards all the major component-averaged quantities (volume, pressure, temperature, etc.) as unknown sinusoidal functions that are linear combinations of $\sin(\omega t)$ and $\cos(\omega t)$. The governing equations used in the method are algebraic and ordinary differential equations (ODEs) written for each individual heat exchanger with the component-averaged quantities as the dependent variables. Examples of the algebraic equations are the equation of state, and the equation of continuity, namely the summation of the mass in all the three (sometimes five) components equals constant. The sinusoidal functions are substituted into the governing equations; the resulting nonlinear terms of $\sin(\omega t)$ and $\cos(\omega t)$ are linearized by using binominal expansion first and then simply neglecting higher order terms. Another way of treating the nonlinearity is to express the nonlinear terms of the major quantities themselves in the equations as Fourier series truncated after the sine and cosine terms. In either way, the linearized equations are simply a few (at most less than dozens) simultaneous algebraic equations. The latter approach is able to

account for the effects of the non-isothermal or transient heat transfer process and pressure drops, which the Schmidt analysis omits. Huang (1992) reported a one-dimensional computer code based on such harmonic analysis method.

In the past decade, fundamental problems of oscillating internal flow and heat transfer with Stirling applications have been experimentally studied to improve analysis and design accuracy. Tang and Cheng (1993) carried out experiments on incompressible periodically reversing pipe flows, and correlated a cycle-averaged Nusselt number in terms of the Reynolds number, dynamic Reynolds number and the nondimensional fluid displacement. Smith and co-workers (Kormhauser and Smith 1989, Smith et al. 1992) did experiments on an apparatus including a piston-cylinder space connected to a dead-end heat exchanger space, and proposed a "complex Nusselt number" model in which heat flux consists of one part proportional to the gas-wall temperature difference plus a second part proportional to the rate of change of the difference. Tew and Geng (1992) gave a review on related experimental projects supported by NASA.

Several researchers have recently begun using two-dimensional (2D) models to simulate Stirling devices numerically. Gedeon (1989) developed a 2D computer code modelling the unsteady laminar flow and heat transfer in Stirling components. He used Darcy's law to simulate the flow and heat transfer in the regenerator, and applied the density-based Beam-Warming scheme (Beam and Warming 1978) as the solution algorithm. This scheme was originally designed for solving compressible (high Mach number) flows, but the Mach number of the flows in a Stirling device is quite low, typically below 0.1. (As will be seen later, the Mach number for the micro-configuration

in the present work is below $1x10^{-4}$.) Density-based numerical schemes, e.g., the Beam-Warming schemes, are inefficient and inaccurate in solving low Mach number or incompressible flows (Karki 1986), and Gedeon reported similar problems encountered in his applications. Ibrahim and co-workers (1991, 1992) also used 2D laminar models to study Stirling components numerically, and suggested a way to correlate the gas-wall heat transfer coefficient under oscillating flow conditions, and they investigated the effects of sudden cross-section changes on heat transfer and friction coefficients. The solution method employed in Ibrahim and co-workers' work was the pressure-based algorithm, SIMPLE, which was initially developed by Patankar (1980) for incompressible flows. By utilizing a 2D model, Kurzweg and Zhao (1993) numerically examined the velocity and pressure fields only within one end chamber of a Stirling microrefrigerator with various orifice configurations, and they recommended a better arrangement of the orifices. They also used the SIMPLE algorithm. Density in the chamber was regarded by them as a function of time only.

In all the above-mentioned 2D numerical studies, the heat-exchanger components were separately considered as open-ended channels (at least at one end), and the velocity boundary conditions (B.C.) at the component entrance or exit were also simply approximated by slug flow and the temperature and density there were taken as uniform. Therefore, the effects of large volume and pressure oscillations were not properly taken into account.

1.3 2D Computational Models and Scope of the Present Work

The main purposes of this work are 1) to propose 2D models for Stirling microrefrigerators, 2) to give a systematic solution methodology suitable for solving the variable-density time-periodic laminar flow and heat transfer within confined regions with moving boundaries, and 3) to numerically investigate the flow and heat transfer phenomena in such configurations.

For computational simplicity, only the three-component configuration is considered in this study. The model adopted here integrates all the three heat exchangers (cooler, heater and regenerator) together, allowing the effect of large pressure and volume variations to be considered properly. To reduce the computational complexity, the regenerator is replaced by narrow channels with linear wall temperature distributions. Since the channels are narrow, there is enough time for the gas flowing in them to adjust its temperature to the desirable wall temperature. Two types of models are studied: single-channel models A1 (Fig. 1.3 (a)) and A2 (Fig. 1.3 (b)); and multichannel models B1 (Fig. 1.4 (a)) and B2 (Fig. 1.4 (b)). In the single-channel models (A1 and A2), the two chambers are connected only by one channel, and all the chamber walls are isothermal. In the multichannel models (B1 and B2), the two chambers are connected by more than one channel. In Models A and B, the piston surface is regarded as insulating; and the wall temperature of the left chamber is set at T_c and that of the right is at Th. The isothermal surfaces are extended into part of the connecting channels to a length "d" in Models A2 and B2. As indicated in the figures, the channel half width is "a", the total channel length is "L", the half chamber width is "b". In either the left

(a) Single-channel model: A1

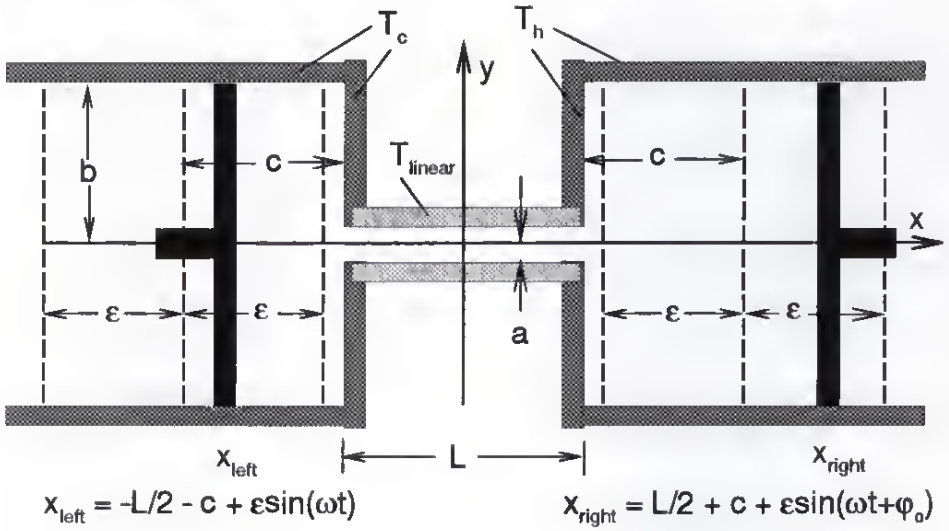

(b) Single-channel model: A2

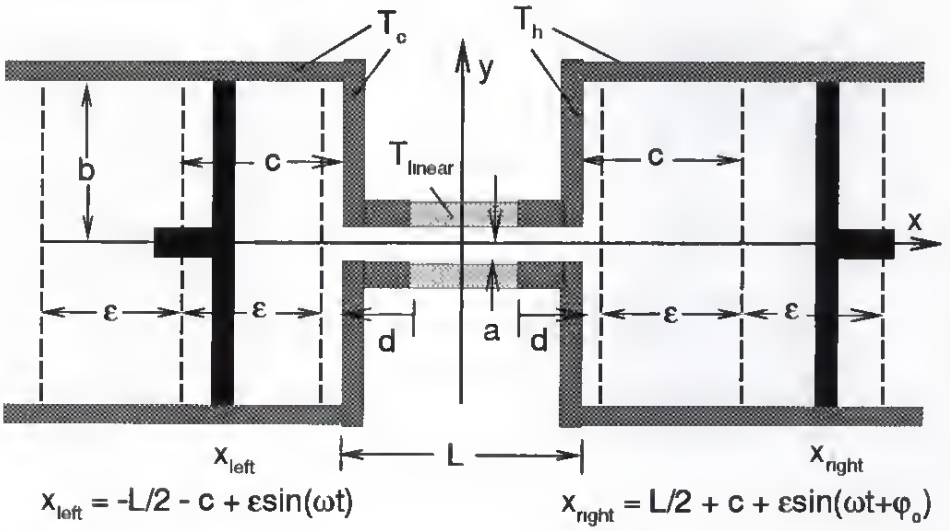

Fig. 1.3 Single-channel models. (a) Model A1; (b) Model A2

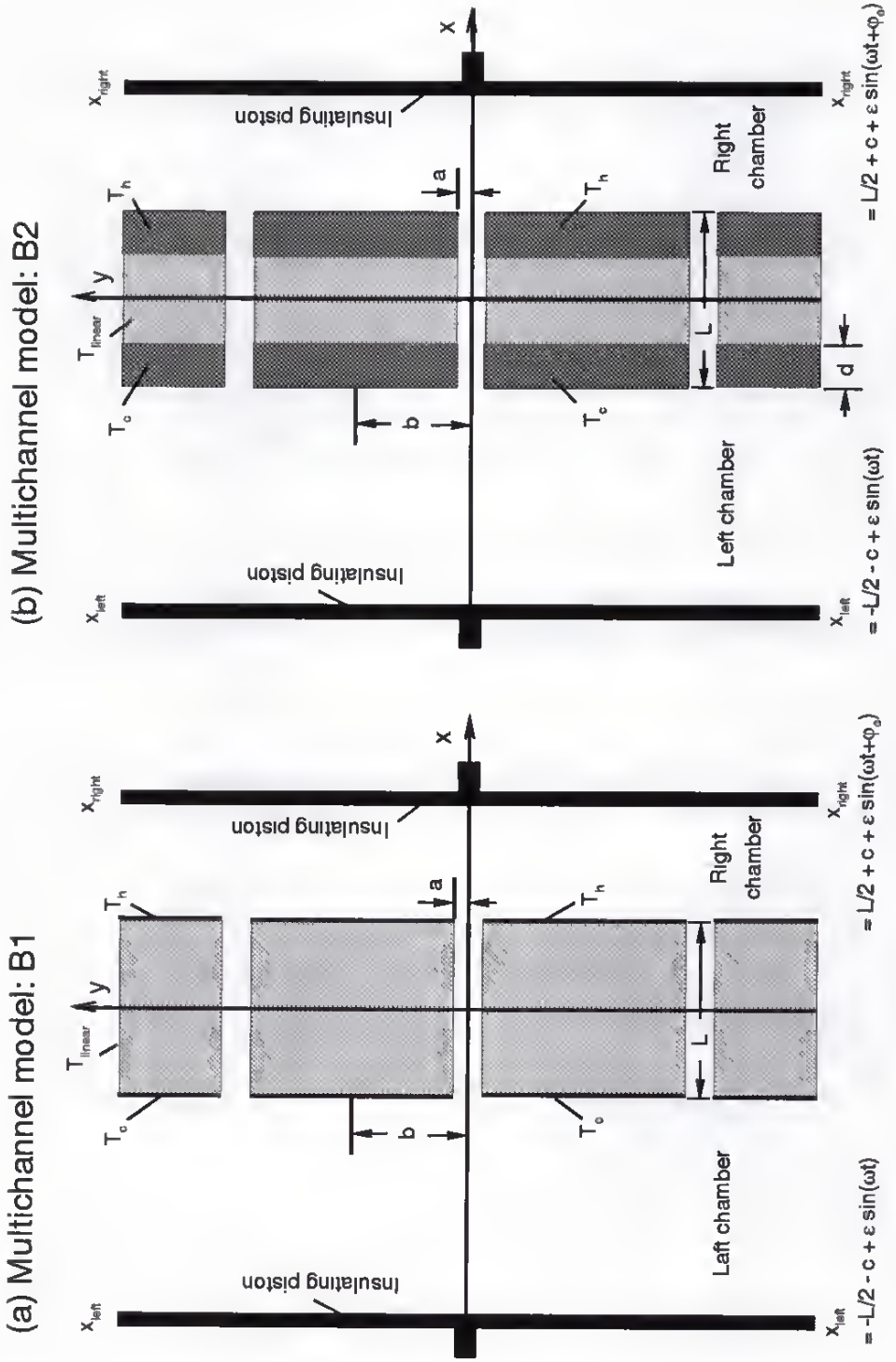

Fig. 1.4 Multichannel models. (a) Model B1; (b) Model B2

or the right chamber, a piston oscillates sinusoidally with an amplitude of "ε" and an angular frequency of "ω". The piston motion in the right (hot) chamber leads that in the left by a phase angle "φ_o" for cooling. The models assume a small clearance of "c-ε" between the piston and the vertical wall. The reasons for this are 1) to avoid difficulties in numerical computations if there is no clearance and 2) to model the actual situation where there is always a clearance and some dead space. Since the models are intended to simulate microrefrigerators, the models are in the centimeter range.

Even though the flow within the 2D models is laminar because of the very small sizes used, numerically solving the pertaining heat and transfer problem still constitutes a difficult task--the challenging elements mentioned before remain the same. Besides, in the variable-density flows with heat transfer, there are significant volumetric changes. The associated thermodynamic pressure, therefore, is many orders larger than the hydrodynamic pressure, and that could result in low computational accuracy and efficiency, and even physically unrealistic solutions. To overcome this problem, a pressure-splitting technique is developed to separate the thermodynamic and hydrodynamic pressures in this study. The Navier-Stokes and energy equations governing the variable-density, oscillatory flow and heat transfer are solved numerically by using the pressure-based algorithm, SIMPLE (Patankar 1980), incorporated with the pressure-splitting technique. Since the domain of interest is bounded by moving pistons, a moving grid technique as used by Demirdžić and Perić (1990) is also incorporated into the algorithm. This study proves that such a methodology is accurate and efficient in solving flow and heat transfer problems like those occurring in Stirling type devices.

By using a code based on the above method, the 2D models of Stirling microrefrigerators are studied. It is found that the model's regeneration and cooling performance are very sensitive to a dimensionless parameter that is the product of the Womersley number squared, Prandtl number, and two geometric parameters. (Womersley number is defined as $\alpha = a\sqrt{\omega}/\sqrt{\nu}$, where ω is the oscillation angular frequency and ν the kinetic viscosity.) This dimensionless parameter should be kept small enough to let the gas passing through the channel adequately adjust the temperature to that of the wall's. A parametric study of the phase angle change is also made and the optimum phase angle is shown to be close to 90°. The effects of varying the temperature ratios between expansion and compression chambers are also examined in this study. The cooling capacity is found to vary linearly with the temperature ratio. Other issues investigated in this study are the effects of changing the channel length and changing the ratio of chamber width to channel width. Some of the findings from the current numerical study agree well with experimental data with actual Stirling refrigerators, and that suggests the proposed 2D models are valuable in helping gain insights into the Stirling microrefrigerators.

The arrangement of this dissertation is as follows. The governing equations and the pressure-splitting technique will be discussed in Chapter 2. Chapter 3 will describe in detail the numerical techniques solving these equations, and the validation of the solution methodology will also be made in Chapter 3. Chapter 4 will focus on the numerical results and discussions, and finally Chapter 5 contains the concluding remarks.

CHAPTER 2
GOVERNING EQUATIONS AND PRESSURE-SPLITTING TECHNIQUE

In this chapter, the governing equations of fluid mechanics and heat transfer appropriate to the problem under consideration are first given. A method is devised to split the pressure into hydrodynamic and thermodynamic parts so that the computational efficiency and accuracy for incompressible (very low Mach number) but variable-density flows with heat transfer are enhanced. The equations and their boundary conditions are nondimensionalized. Then the governing equations are cast into a form that is suitable for the numerical solution algorithm to be used. At the end of this chapter, dimensional analysis is carried out for the cooling power, heating power and the rate of work input in the Stirling microrefrigerator models.

2.1 Governing Equations

The governing equations of viscous, variable-density, unsteady flows and heat transfer with negligible body forces in domains with deformable moving boundaries can be written in an integral form as (Hansen 1967):

Conservation of mass,

$$\frac{d}{dt}\int_{\forall(t)}\rho\, d\forall + \oint_{S(t)}\rho(\vec{V}-\vec{V}_b)\cdot\hat{n}\, dS = 0\ , \tag{2.1}$$

Conservation of momentum,

$$\frac{d}{dt}\int_{\forall(t)}\rho\vec{V}d\forall + \oint_{S(t)}\rho\vec{V}(\vec{V}-\vec{V}_b)\cdot\hat{n}\, dS = \oint_{S(t)}(-p\tilde{I}+\tilde{\tau})\cdot\hat{n}\, dS\ , \tag{2.2}$$

Conservation of energy,

$$\frac{d}{dt}\int_{\forall(t)}\rho E d\forall + \oint_{S(t)}\rho E(\vec{V}-\vec{V}_b)\cdot\hat{n}\, dS = -\oint_{S(t)}\vec{q}\cdot\hat{n}\, dS + \oint_{S(t)}\vec{V}\cdot(-p\tilde{I}+\tilde{\tau})\cdot\hat{n}\, dS. \tag{2.3}$$

In the above equations, $\forall(t)$ represents the control volume, S(t) the moving control surface, $\vec{V}_b$ the velocity of the control surface, and $\hat{n}$ the outward unit normal to the control surface; ρ is the density of the fluid, $\vec{V}$ the velocity of the flow, E the total energy of the fluid per unit mass, p the pressure, $\tilde{I}$ the identity stress tensor, $\tilde{\tau}$ the deviatoric stress tensor, and $\vec{q}$ the conduction heat flux vector. Here the assumption of Newtonian fluid is used.

Notice that if the velocity of the control surface is the same as the fluid velocity there, then the Lagrangian approach is taken; if the velocity of the control surface is zero, then the Eulerian approach is taken. Otherwise the viewpoint is neither Lagrangian nor Eulerian, as happens in this study.

Since the body force is negligible, potential energy is negligible, too. The total energy is then given as

$$E = e + \frac{1}{2}\vec{V}\cdot\vec{V}\ , \tag{2.4}$$

where $\frac{1}{2}\vec{V}\cdot\vec{V}$ is the kinetic energy per unit mass, and e the internal energy per unit mass. The internal energy for a perfect gas is given by,

$$e = c_v T. \tag{2.5}$$

Here c_v is the specific heat at constant volume, and T the absolute temperature.

According to Stokes' hypothesis, the deviatoric stress tensor is

$$\tilde{\tau} = \mu[\nabla\vec{V} + (\nabla\vec{V})^T] - \mu\frac{2}{3}(\nabla\cdot\vec{V})\tilde{I}\,, \tag{2.6}$$

where the superscript "T" represents the transposition of a tensor, and μ is the molecular viscosity of the fluid.

The equation of state gives the relationship among p, ρ and T, and reads

$$p = \rho RT. \tag{2.7}$$

where R is the gas constant.

In the energy equation, the conduction heat flux is given by Fourier's law

$$\vec{q} = -k\,\nabla T\,, \tag{2.8}$$

where k is the coefficient of thermal conductivity.

Viscosity is determined by using Sutherland's formula

$$\mu = \mu_r \frac{T_r + T_\mu}{T + T_\mu}\left(\frac{T}{T_r}\right)^{3/2}, \tag{2.9}$$

in which T_r is some reference temperature, μ_r the viscosity of the fluid at the reference temperature, and T_μ a constant that depends on the fluid.

Thermal conductivity k can be determined from viscosity μ and specific heat at

constant pressure

$$k = \frac{\mu\, c_p}{Pr}\,, \tag{2.10}$$

where Pr is the Prandtl number, which is usually a constant for a specific fluid. For a perfect gas,

$$c_p - c_v = R, \tag{2.11}$$

and

$$c_p = \gamma c_v\,, \tag{2.12}$$

where γ is called the ratio of specific heats, and is a constant for a given gas.

2.2 Separation of Hydrodynamic and Thermodynamic Pressures

The pressure $p(x,y,z,t)$ consists of hydrodynamic pressure, denoted by p^h, and thermodynamic pressure, denoted by p^t, i.e.,

$$p(x,y,z,t) = p^h + p^t. \tag{2.13}$$

The hydrodynamic pressure is related to the inertial and viscous forces and is usually a function of both time and space, so

$$p^h = p^h(x,y,z,t); \tag{2.14}$$

and the thermodynamic pressure is related to the volumetric changes and temperature variations. At very low Mach numbers, the thermodynamic pressure is a function of time only, i.e.,

$$p^t = p^t(t), \tag{2.15}$$

Consequently,

$$\frac{p^h}{p^t} \sim O(M^2) \ll 1 \ . \tag{2.16}$$

In numerically solving the momentum equation (2.2), pressure gradient terms like $\partial p/\partial x$ need to be approximated. As a demonstration, consider a 1D problem where the pressure gradient is dp/dx. As shown in Fig. 2.1, the pressure gradient at $x_{i+1/2} = (x_i + x_{i+1})/2$, denoted as $(dp/dx)_{i+1/2}$, is estimated by

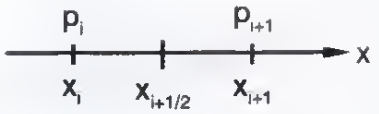

Fig. 2.1 Illustrative 1D discretization

$$\left(\frac{dp}{dx}\right)_{i+1/2} = \frac{p_{i+1} - p_i}{x_{i+1} - x_i} \ , \tag{2.17}$$

where

$$p_i = p^h{}_i + p^t, \tag{2.18}$$

$$p_{i+1} = p^h{}_{i+1} + p^t, \tag{2.19}$$

From the above discussion, p^t is independent of x and is several orders larger than p^h. So what is done in Eq. (2.17) is subtracting two very close numbers from one another with the difference between them being many orders smaller than the two numbers themselves. If the computer used does not have enough digits, large round-off errors and even catastrophic cancellation may occur in the calculation and the numerical solutions are erroneous (Golub and Ortega 1992). Although using double-precision arithmetic in

computations can increase the accuracy, a price of more computer memory, storage and CPU time must be paid.

Wei Shyy * suggested that effort should be made in order to find a way of separating hydrodynamic and thermodynamic pressures so that the computing accuracy and efficiency could be increased. The rationale follows. Substituting Eqs. (2.18) and (2.19) into Eq. (2.17) yields

$$(\frac{dp}{dx})_{i+1/2} = \frac{(p^h_{i+1} + p^t) - (p^h_i + p^t)}{x_{i+1} - x_i} = \frac{p^h_{i+1} - p^h_i}{x_{i+1} - x_i} = (\frac{dp^h}{dx})_{i+1/2} . \qquad (2.20)$$

Then the problem of catastrophic cancellation does not exist anymore, and therefore the computing accuracy is enhanced without using double-precision arithmetic. The computer CPU time, memory as well as storage are saved. Now the question is how to determine p^h and p^t.

Such a method is developed in the present study. First consider how to determine the hydrodynamic pressure p^h. It can be seen from Eq. (2.20) that the pressure p appearing in the momentum equation (2.2) can now be replaced by the hydrodynamic pressure p^h and therefore p^h is solved by using the pressure-based SIMPLE algorithm, which will be discussed in Chapter 3. It should be noted that the total pressure appearing in the energy equation (2.3) has nothing to do with the pressures splitting procedures because the pressure there is replaced with ρRT via the equation of state (2.7).

Next consider the thermodynamic pressure p^t. It can be determined by using the

---

*Personal communication, 1994.

equation of state and the total mass of the whole system, and the procedure follows. From Eqs. (2.7) and (2.13), the density is given by

$$\rho = \frac{p}{RT} = \frac{p^h + p^t}{RT} . \tag{2.21}$$

The total mass of the entire system is known at any time instant, and

$$\text{Total Mass} = \int_{\forall(t)} \rho(x,y,z,t) d\forall = \int_{\forall(t)} \frac{p^h(x,y,z,t) + p^t(t)}{RT(x,y,z,t)} d\forall . \tag{2.22}$$

Therefore,

$$p^t(t) = \frac{1}{\int_{\forall(t)} \frac{1}{RT} d\forall} [\text{Total Mass} - \int_{\forall(t)} \frac{p^h}{RT} d\forall] . \tag{2.23}$$

In this way, the hydrodynamic and thermodynamic pressures, which are of different physical meaning and of different order of magnitudes, are determined separately, and consequently the computing accuracy and/or efficiency is increased.

2.3 Boundary Conditions

The symmetry of the geometry and the boundary conditions under consideration makes the solution also symmetric about the x-axis (see Figs.1.3 and 1.4). Numerical calculation takes the advantage of the symmetry by considering only half the domain of interest as the computational domain with symmetry boundary conditions being applied at the symmetry line, as a result the computing effort needed is greatly reduced. For example, the upper half domain of interest in the present work is taken as the

computational domain. In what follows, the boundary conditions for Model B2 (Fig. 1.4 (b)) are listed.

Velocity boundary conditions are as follows:

$x = x_{left}$, $0 \le y \le b$, left piston wall, no-slip:

$$u = u_{left} = -\varepsilon\omega\sin(\omega t), \quad v = 0. \tag{2.24}$$

$x_{left} < x < -L/2$, $y = b$, imaginary boundary, symmetry:

$$\partial u/\partial y = 0, \quad v = 0.$$

$x = -L/2$, $a < y \le b$, vertical wall of the left chamber, no-slip:

$$u = 0, \quad v = 0.$$

$-L/2 \le x \le L/2$, $y = a$, upper channel wall, no-slip:

$$u = 0, \quad v = 0.$$

$x = L/2$, $a < y \le b$, vertical wall of the right chamber, no-slip:

$$u = 0, \quad v = 0.$$

$L/2 < x < x_{right}$, $y = b$, imaginary boundary, symmetry:

$$\partial u/\partial y = 0, \quad v = 0.$$

$x = x_{right}$, $0 \le y \le b$, right piston, no-slip:

$$u = u_{right} = -\varepsilon\omega\sin(\omega t + \varphi_o), \quad v = 0. \tag{2.25}$$

$x_{left} < x < x_{right}$, $y = 0$, symmetry:

$$\partial u/\partial y = 0, \quad v = 0.$$

The temperature boundary conditions are as follows:

$x = x_{left}$, $0 \le y \le b$: $\partial T/\partial x = 0$.

$x_{left} < x < -L/2$, $y = b$: $\partial T/\partial y = 0$.

$x = -L/2,\ a < y \le b$: $T = T_c$.

$-L/2 \le x < -L/2+d,\ y=a$: $T = T_c$.

$-L/2+d \le x \le L/2-d,\ y=a$: $T = T_c + (T_h - T_c)\,(x + L/2 - d)/(L - 2d)$.

$L/2-d < x \le L/2,\ y=a$: $T = T_h$.

$x = L/2,\ a < y \le b$: $T = T_h$.

$L/2 < x < x_{right},\ y=b$: $\partial T/\partial y = 0$.

$x = x_{right},\ 0 \le y \le b$: $\partial T/\partial x = 0$.

$x_{left} < x < x_{right},\ y = 0$: $\partial T/\partial y = 0$.

Here the boundary conditions for velocity and temperature only include two types, Dirichlet and Neumann, and all the Neumann boundary conditions here have zero gradients. Around the entire boundary, the velocity component normal to the boundary is always known.

Pressure does not requires explicit boundary conditions here. As will be discussed in the next chapter, the numerical algorithm adopted in this study does not need explicit pressure boundary conditions when the velocity normal to the boundary is given.

2.4 Nondimensionalization of Governing Equations and Boundary Conditions

In the analysis or numerical computation of a physical problem, the governing equations and boundary conditions are usually nondimensionalized. The reasons for this are twofold: first, by doing so the nondimensional parameters governing the physical problem are obtained; second, computation convenience is also achieved by using nondimensional quantities. The governing equations and boundary conditions are

nondimensionalized as follows.

First reference quantities are properly chosen:

Reference length: $L_r = a$ (channel half width);

Reference time: $t_r = 1/\omega$ (ω = angular frequency of the piston oscillation);

Reference velocity: $U_r = L_r/t_r = a\omega$. The reference velocity is defined in terms of the reference length and reference time and cannot be arbitrarily chosen;

Reference temperature: T_r. It should be chosen such that it is as close as possible to the temporal and spatial average temperature;

Reference density: ρ_r. Like T_r, the reference density is also chosen so that it is as close as possible to the temporal and spatial average density;

Reference viscosity: $\mu_r = \mu(T_r)$.

Then the nondimensional quantities, which are denoted by bars, can be defined as

$$\bar{x}_i = \frac{x_i}{L_r} = \frac{x_i}{a}, \qquad \bar{t} = \frac{t}{t_r} = \omega t, \qquad \bar{u}_i = \frac{u_i}{U_r} = \frac{u_i}{a\omega}, \qquad \bar{\rho} = \frac{\rho}{\rho_r}, \qquad \bar{T} = \frac{T}{T_r},$$

$$\bar{\mu} = \frac{\mu}{\mu_r}, \qquad \bar{e} = \frac{e}{U_r^2}, \qquad \bar{E} = \frac{E}{U_r^2} = \bar{e} + \frac{1}{2}\vec{\bar{V}}\cdot\vec{\bar{V}}, \qquad \bar{\tau} = \frac{\tau}{\mu_r \frac{U_r}{L_r}}.$$

Special care should be taken in nondimensionalizing the hydrodynamic and thermodynamic pressures because of their inherent different scales. The corresponding nondimensional quantities are defined as

$$\bar{p}^h = \frac{p^h}{\rho_r U_r^2} ,$$

$$\bar{p}^t = \frac{p^t}{\rho_r R T_r} .$$

For convenience from now on the bars over the nondimensional quantities will be dropped with the understanding that nondimensional quantities are used, unless otherwise mentioned.

Finally, the above nondimensional quantities are substituted into the governing equations and boundary conditions. The nondimensional equations are:

Conservation of mass,

$$\frac{d}{dt}\int_{\forall(t)} \rho \, d\forall + \oint_{S(t)} \rho(\vec{V}-\vec{V}_b)\cdot\hat{n}\,dS = 0 , \tag{2.26}$$

Conservation of momentum,

$$\frac{d}{dt}\int_{\forall(t)} \rho\vec{V}\,d\forall + \oint_{S(t)} \rho\vec{V}(\vec{V}-\vec{V}_b)\cdot\hat{n}\,dS = -\oint_{S(t)} p^h\hat{n}\,dS + \frac{1}{\alpha^2}\oint_{S(t)} \bar{\tau}\cdot\hat{n}\,dS , \tag{2.27}$$

Conservation of energy,

$$\begin{aligned}\frac{d}{dt}\int_{\forall(t)} \rho T\,d\forall + \oint_{S(t)} \rho T(\vec{V}-\vec{V}_b)\cdot\hat{n}\,dS &= \frac{\gamma}{Pr\,\alpha^2}\oint_{S(t)} \nabla(\mu T)\cdot\hat{n}\,dS \\ -(\gamma-1)\oint_{S(t)} \rho T\vec{V}\cdot\hat{n}\,dS &+ \frac{\gamma(\gamma-1)M^2}{\alpha^2}\oint_{S(t)} \vec{V}\cdot\bar{\tau}\cdot\hat{n}\,dS \\ + \gamma(\gamma-1)M^2\Big[\frac{d}{dt}\int_{\forall(t)} \frac{1}{2}\rho\vec{V}\cdot\vec{V}\,d\forall &+ \oint_{S(t)} \frac{1}{2}\rho\vec{V}\cdot\vec{V}(\vec{V}-\vec{V}_b)\cdot\hat{n}\,dS\Big] ,\end{aligned} \tag{2.28}$$

Equation of state,

$$p^t + \gamma M^2 p^h = \rho T \,. \tag{2.29}$$

Here one should notice the following two points: 1) the pressure in the momentum equation (2.27) is just the hydrodynamic pressure p^h, and 2) the form of the nondimensional equation of state (2.29).

The nondimensional parameters in these equations are:

Prandtl number: $\quad Pr = (\mu c_p / k)_r = \nu_r / \kappa_r \,,$

Ratio of specific heats: $\quad \gamma = c_p / c_v \,,$

Mach number: $\quad M = a\omega/(\gamma R T_r)^{1/2} = U_r/(\gamma R T_r)^{1/2}$

$= $ (reference speed) / (speed of sound at T_r), (2.30)

Womersley number: $\quad \alpha = a\,(\rho_r \omega/\mu_r)^{1/2} = a\,(\omega/\nu_r)^{1/2}.$ (2.31)

This parameter characterizes oscillatory flows, and is also known to be Stokes number. Instead of the above parameter, another parameter is also used in the literature. The latter is defined as

$$Va = a^2 \omega/\nu_r = \alpha^2 = L_r U_r/\nu_r \,. \tag{2.32}$$

It is called the Valensi number or nondimensional frequency (Ahn and Ibrahim 1991), or oscillating Reynolds number (Tew 1987).

For simplicity, the nondimensional velocity and temperature boundary conditions will not be listed here. The nondimensional parameters resulting from the boundary conditions are b/a, c/a, d/a, ε/a, L/a, T_c/T_r, T_h/T_r and φ_o.

Since T is used as the dependent variable to be solved for in the energy equation (2.28), quantities p, e and consequently E are all expressed in terms of T there. The second term, including the minus sign "-", on the right-hand side (RHS) of the equation

is the rate at which work is done to compress the gas and therefore the rate at which the internal energy increases owing to compression; the third term on the RHS is the rate of dissipation of mechanical energy due to viscosity; and the last terms in the square brackets on the RHS are related to kinetic energy. In this study the dissipation term and the terms related to kinetic energy are neglected because they all include the factor M^2 and M here is always smaller than 10^{-4}. Therefore, the energy equation is simplified, without loss of computational accuracy, to

$$\frac{d}{dt}\int_{\forall(t)} \rho T d\forall + \oint_{S(t)} \rho T(\vec{V}-\vec{V}_b)\cdot\hat{n}dS = \frac{\gamma}{Pr\alpha^2}\oint_{S(t)} \nabla(\mu T)\cdot\hat{n}dS - (\gamma-1)\oint_{S(t)} \rho T\vec{V}\cdot\hat{n}dS. \tag{2.33}$$

2.5 General Form of the Governing Equations

Any of the integral equations presented in the preceding section can be cast into the following general form

$$\frac{d}{dt}\int_{\forall(t)} \rho\phi d\forall + \oint_{S(t)} \rho\phi(\vec{V}-\vec{V}_b)\cdot\hat{n}dS = \oint_{S(t)} (\Gamma\nabla\phi)\cdot\hat{n}dS + \int_{\forall(t)} \zeta d\forall , \tag{2.34}$$

where Γ is the diffusion coefficient, ζ the source per unit volume. Each specific integral equation corresponds to a specific set of ϕ, Γ and ζ, which are tabulated in Table 2.1 for two dimensions.

The first term on the left-hand side (LHS) of Eq. (2.34) is the rate of change of the extensive property inside the control volume, that corresponds to the intensive property ϕ; the second term on the LHS is the rate of efflux across the control surface,

and called the convection term. The first term on the RHS of the equation is called the rate of diffusion, and the second term on the RHS the source term. Anything that cannot be put into the three terms mentioned above is put into the source term, as is the case in the momentum and energy equations.

Table 2.1 Terms in the governing equation (2.34)

	ϕ	Γ	ζ
Continuity	1	$\mathbb{F}$	0
u-Momentum	u	$\frac{\mu}{\alpha^2}$	$-\frac{\partial p^h}{\partial x}+\frac{1}{3}\frac{\partial}{\partial x}(\mu\frac{\partial u}{\partial x})-\frac{2}{3}\frac{\partial}{\partial x}(\mu\frac{\partial v}{\partial y})+\frac{\partial}{\partial y}(\mu\frac{\partial v}{\partial x})$
v-Momentum	v	$\frac{\mu}{\alpha^2}$	$-\frac{\partial p^h}{\partial y}+\frac{1}{3}\frac{\partial}{\partial y}(\mu\frac{\partial v}{\partial y})-\frac{2}{3}\frac{\partial}{\partial y}(\mu\frac{\partial u}{\partial x})+\frac{\partial}{\partial x}(\mu\frac{\partial u}{\partial y})$
Energy	T	$\frac{\gamma\mu}{Pr\ \alpha^2}$	$-(\gamma-1)[\ \frac{\partial(\rho uT)}{\partial x}+\frac{\partial(\rho vT)}{\partial y}\ ]$

2.6 Dimensional Analysis

The physical quantities of much interest with the computational models are: cooling power, heating power and rate of work input, the definitions of which will be given in the next chapter. Since they all have the dimension of power, they are generally

denoted as $\mathcal{P}$ for the dimensional analysis purpose. For the flow and heat transfer problem under consideration, there are four basic dimensions, [length], [time], [mass] and [temperature]. Here "[ ]" means "the dimension of". The four basic quantities, which include all these basic dimensions and at the same time never make a nondimensional quantity themselves, are chosen as L_r, t_r, ρ_r and T_r. They were used as the references in the previous nondimensionalization of the governing equations and boundary conditions. The quantity $\mathcal{P}$ is nondimensionalized by dividing it by $L_r^5 t_r^{-3} \rho_r T_r^0$, i.e., $\rho_r a^5 \omega^3$. From the Π theorem (Fox and McDonald 1978), we have

$$\mathcal{P} / (\rho_r a^5 \omega^3) = \mathcal{F}\{Pr, \gamma, M, \alpha, \varphi_o, T_c/T_r, T_h/T_r, b/a, c/a, d/a, \varepsilon/a, L/a\}. \qquad (2.35)$$

CHAPTER 3
NUMERICAL TECHNIQUES AND CODE VALIDATION

The integral equations discussed in the last chapter need to be solved numerically for the specified boundary conditions. The gas flow under consideration is still incompressible even though the density of the gas changes considerably with space and time. This is because the Mach number here is very small, and therefore the density variation is not caused by pressure gradients, but by temperature gradients and volumetric changes. So the flow should be called incompressible variable-density flow, and the SIMPLE algorithm (Patankar 1980), which was originally developed for incompressible flows and heat transfer, can be adopted as the proper solution algorithm. To solve the problem with moving boundaries, the moving grid technique by Demirdžić and Perić (1990) is incorporated into the SIMPLE algorithm. The pressure-splitting method proposed in the last chapter and the code developed accordingly are validated with some cases whose solutions are known beforehand so that the code can be used for production runs.

3.1 Numerical Grid Generation

In order for the integral equations to be solved numerically, the entire domain is discretized with grids into a system of subdomains, or cells. At every time step, new

grids are generated according to the oscillating-piston locations. Owing to the rectangular nature of the boundaries of the models under consideration, Cartesian rectangular grids are used. Figures 3.1 (a) and 3.1 (b) show two typical grid distributions at time instants $\omega t = \pi/4$ and π, respectively. The domain is decomposed into three blocks with each in the left chamber, the channel and the right chamber. The total number of grid points in each direction within a particular block is kept constant and the grids move and deform only in the x-direction but not in the y-direction.

Consider the grid distribution in the x-direction. Suppose there are N grid points to be distributed along a line segment parallel to the x-axis, starting at $x=x_1$ and ending at $x=x_N$, with the first and last grid spacings being specified as Δx_o and Δx_f, respectively (Fig. 3.2). Grid points are distributed according to the hyperbolic tangent distribution given by Thompson et al. (1985) as follows.

First define

$$G = \frac{\sqrt{\Delta x_o \Delta x_f}}{\frac{x_N - x_1}{N-1}}, \tag{3.1}$$

and

$$H = \sqrt{\frac{\Delta x_f}{\Delta x_o}}. \tag{3.2}$$

Then solve one of the following nonlinear equations for the parameter δ by using the Newton-Raphson method (Hornbeck 1982):

(a)

(b)

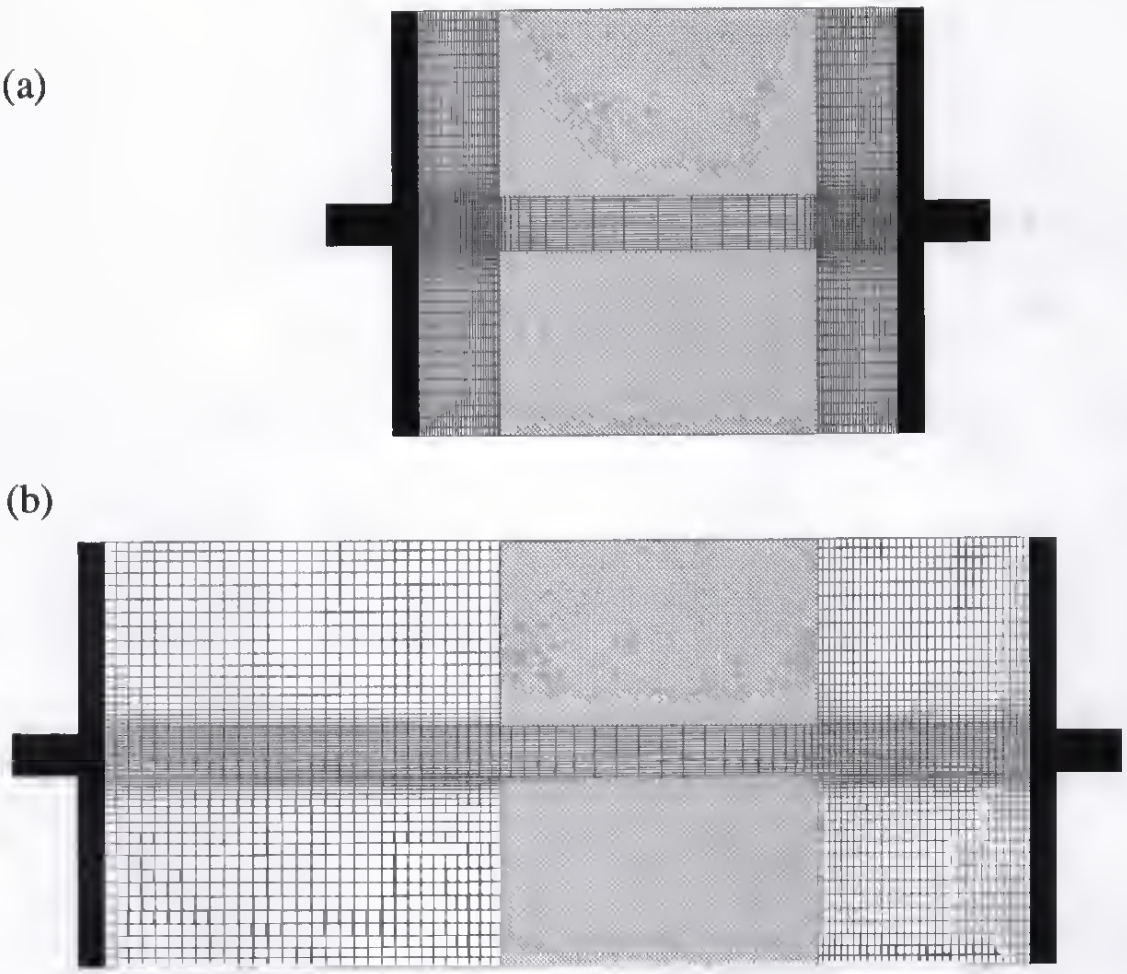

Fig. 3.1 Two typical grids. (a) $\omega t = \pi/4$; (b) $\omega t = \pi$.

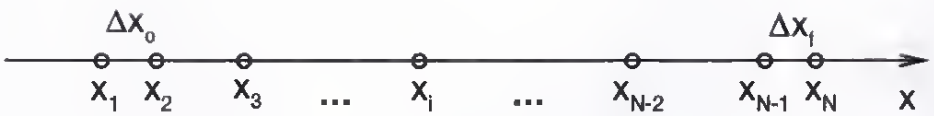

Fig. 3.2 1D grids

$$\frac{\sinh\delta}{\delta} = \frac{1}{G} \qquad \text{for } G < 1 \,, \tag{3.3}$$

$$\frac{\sin\delta}{\delta} = \frac{1}{G} \qquad \text{for } G > 1 \,. \tag{3.4}$$

The i-th grid is distributed at

$$x_i = x_1 + \frac{g_i}{H+(1-H)g_i}(x_N - x_1) \,, \tag{3.5}$$

where

$$g_i = \frac{1}{2}\{1 + \frac{\tanh[\delta(\frac{i-1}{N-1} - \frac{1}{2})]}{\tanh\frac{\delta}{2}}\} \,. \tag{3.6}$$

For each chamber block, either x_N or x_1 varies with time due to piston oscillations. The two end spacings are given in terms of the instantaneous average grid spacing at each time instant so that a good moving grid distribution is achieved. The hyperbolic tangent distribution is also used for generating the grid in the channel block with each end spacing being the same as the respective adjacent end spacing of the chamber block, resulting in a smooth grid distribution near the chamber and channel interfaces. Similar procedures are applied to generate grids along the y-direction.

3.2 Discretization of the Governing Equations

As mentioned earlier, the governing equations need to be discretized on a finite number of cells (i.e., finite volumes), so that they can be solved numerically. The

staggered grid layout is adopted here to avoid the pressure-velocity decoupling (see Patankar 1980). Figure 3.3 shows that the control volumes for scalar quantities ρ, p and T are the same and the quantities are located at the centers of the control volumes. A typical scalar control volume is highlighted in the figure. Velocity components (u and v) are located at the interfaces of the scalar control volumes. As a result, the u control volumes shift in the x-direction by half cell distance from the scalar control volumes, and similarly v control volumes also shift in the y-direction by half cell distance. Figure 3.4 shows a typical u control volume and a typical v control volume. Each of the quantities indicated there is regarded as the average value over the relevant control volume. It can be seen from the above discussion that for the 2D staggered grid layout, there are three sets of control volumes: one set for all scalar quantities, and the other two for the two velocity components.

The general equation (2.34) is taken here as an example to demonstrate the procedures for discretizing the governing equations. Consider a cell centered at point P with neighboring cells centered at points N, W, S and E (as shown in Fig. 3.5). The midpoints of the interfaces between cell P and each of its neighboring cells are denoted by lower case letters n, w, s and e. As mentioned in the last section, the grid points move in the x-direction. So Fig. 3.5 also shows the grid velocities: $(u_g)_e$--at the east interface, and $(u_g)_w$--at the west interface. The grid velocities are evaluated by using first order finite difference based on the grid coordinates at current and last time levels. From Eq. (2.34), the integral equation for the general quantity ϕ over cell P is

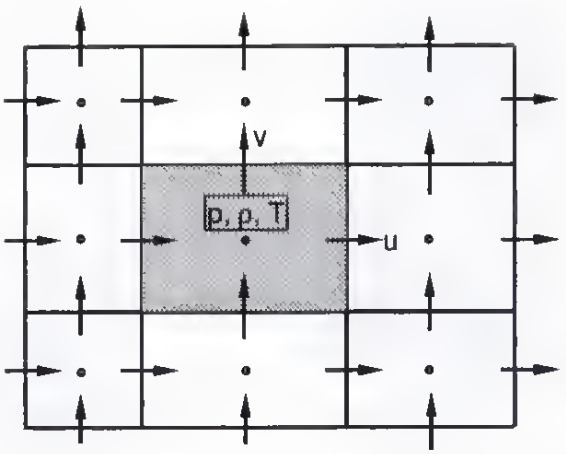

Fig. 3.3 Control volumes for scalar quantities

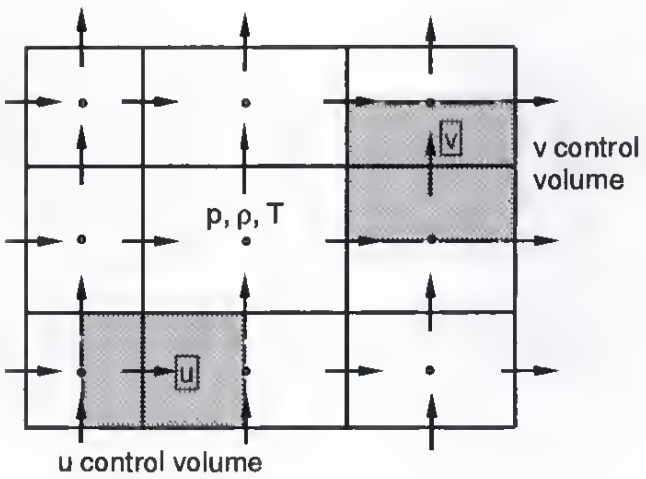

Fig. 3.4 Staggered u and v control volumes

$$\frac{d}{dt}\int_{\forall_P(t)} \rho\phi d\forall + \oint_{S_P(t)} \rho\phi(\vec{V}-\vec{V}_b)\cdot\hat{n}dS = \oint_{S(t)} \Gamma\nabla\phi\cdot\hat{n}dS + \int_{\forall_P(t)} \zeta d\forall \,, \qquad (3.7)$$

where the subscript "P" denotes the quantity of cell P.

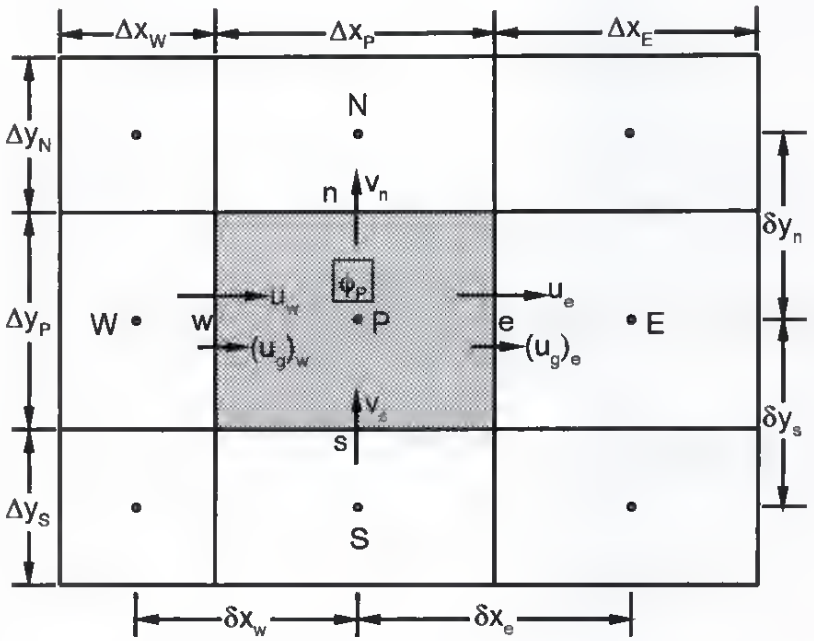

Fig. 3.5 Schematic of a general cell for ϕ at point P

Consider the rate-of-change term first. In reference to Fig. 3.5, this term can be discretized as

$$\frac{d}{dt}\int_{\forall_P(t)} \rho\phi d\forall = \frac{\rho_P\phi_P\forall_P - \rho_P^o\phi_P^o\forall_P^o}{\Delta t} \,, \qquad (3.8)$$

where Δt is the time step size, $\forall_P$ the cell volume, and the superscript "o" represents a quantity at the last time level. Here only a 2D case is considered, so

$$\forall_P = A_P = \Delta x_P \Delta y_P , \tag{3.9}$$

and consequently,

$$\frac{d}{dt}\int_{\forall_P(t)} \rho\phi d\forall = \frac{\rho_P\phi_P A_P - \rho_P^o\phi_P^o A_P^o}{\Delta t} . \tag{3.10}$$

The convection term is discretized as

$$\begin{aligned}\oint_{S_P(t)} \rho\phi(\vec{V}-\vec{V}_b)\cdot\hat{n}dS = {} & \rho_e\phi_e(u-u_g)_e\Delta y_P - \rho_w\phi_w(u-u_g)_w\Delta y_P \\ & + \rho_n\phi_n v_n\Delta x_P - \rho_s\phi_s v_s\Delta x_P .\end{aligned} \tag{3.11}$$

Define mass fluxes through the cell faces

$$F_e = [\rho(u-u_g)]_e\,\Delta y_P , \quad F_w = [\rho(u-u_g)]_w\,\Delta y_P , \tag{3.12}$$

$$F_n = (\rho v)_n\,\Delta x_P , \quad F_s = (\rho v)_s\,\Delta x_P , \tag{3.13}$$

then

$$\oint_{S_P(t)} \rho\phi(\vec{V}-\vec{V}_b)\cdot\hat{n}dS = F_e\phi_e - F_w\phi_w + F_n\phi_n - F_s\phi_s . \tag{3.14}$$

The diffusion term is then discretized as

$$\begin{aligned}\oint_{S_P(t)} \Gamma\nabla\phi\cdot\hat{n}dS = {} & (\Gamma\frac{\partial\phi}{\partial x})_e\Delta y_p - (\Gamma\frac{\partial\phi}{\partial x})_w\Delta y_p \\ & + (\Gamma\frac{\partial\phi}{\partial y})_n\Delta x_p - (\Gamma\frac{\partial\phi}{\partial y})_s\Delta x_p .\end{aligned} \tag{3.15}$$

The first derivatives in the above expressions are approximated by first order finite differencing, e.g.,

$$(\frac{\partial\phi}{\partial x})_e = \frac{\phi_E - \phi_P}{\delta x_e} \ . \tag{3.16}$$

Thus one has,

$$\begin{aligned} \text{RHS of Eq.(3.15)} &= \Gamma_e\frac{\Delta y_P}{\delta x_e}(\phi_E-\phi_P)-\Gamma_w\frac{\Delta y_P}{\delta x_w}(\phi_P-\phi_W) \\ &\quad +\Gamma_n\frac{\Delta x_P}{\delta y_n}(\phi_N-\phi_P)-\Gamma_s\frac{\Delta x_P}{\delta y_s}(\phi_P-\phi_S) \\ &= D_e(\phi_E-\phi_P)-D_w(\phi_P-\phi_W)+D_n(\phi_N-\phi_P)-D_s(\phi_P-\phi_S) \ , \end{aligned} \tag{3.17}$$

where the diffusion fluxes are defined as

$$D_e = \Gamma_e\frac{\Delta y_P}{\delta x_e} \ , \quad D_w = \Gamma_w\frac{\Delta y_P}{\delta x_w} \ , \quad D_n = \Gamma_n\frac{\Delta x_P}{\delta y_n} \ , \quad D_s = \Gamma_s\frac{\Delta x_P}{\delta y_s} \ . \tag{3.18}$$

The discretization of the source term is straightforward,

$$\int_{\forall_P(t)} \zeta d\forall = \forall_P\zeta_P = A_P\zeta_P \ . \tag{3.19}$$

Substituting all the discretized terms into the integral equation (3.7) gives

$$\begin{aligned} &\frac{\rho_P A_P\phi_P - \rho_P^\circ A_P^\circ\phi_P^\circ}{\Delta t}+F_e\phi_e-F_w\phi_w+F_n\phi_n-F_s\phi_s = \\ &D_e(\phi_E-\phi_P)-D_w(\phi_P-\phi_W)+D_n(\phi_N-\phi_P)-D_s(\phi_P-\phi_S)+A_P\zeta_P \ . \end{aligned} \tag{3.20}$$

Notice that the fully implicit first order backward Euler scheme is used. In the above equation, the ϕ values at cell faces, i.e. ϕ_e, ϕ_n, ϕ_w and ϕ_s, have to be expressed in terms of the values at cell centers, i.e. ϕ_E, ϕ_N, ϕ_W and ϕ_S, since the latter are regarded as unknowns to be solved. Convection schemes are needed to do this (for

details, see Patankar 1980, Shyy 1994). Applying a convection scheme to the above equation and then collecting terms gives the algebraic equation for ϕ in the final form:

$$a_P\phi_P = a_E\phi_E + a_W\phi_W + a_N\phi_N + a_S\phi_S + B = \sum_{nb} a_{nb}\phi_{nb} + B \,, \tag{3.21}$$

where, for compactness, the subscript "nb" denotes evaluations at the neighboring points of point P, and the coefficients are defined by

$$a_E = D_e C(|Pec_e|) + \max\{-F_e, 0\}, \tag{3.22}$$

$$a_W = D_w C(|Pec_w|) + \max\{F_w, 0\}, \tag{3.23}$$

$$a_N = D_n C(|Pec_n|) + \max\{-F_n, 0\}, \tag{3.24}$$

$$a_S = D_s C(|Pec_s|) + \max\{F_s, 0\}, \tag{3.25}$$

$$B = \zeta_P A_P + a_P^o \phi_P^o \,, \tag{3.26}$$

$$a_P^o = \frac{(\rho A)_P^o}{\Delta t} \,, \tag{3.27}$$

$$a_P = a_E + a_W + a_N + a_S + a_P^o = \sum_{nb} a_{nb} + a_P^o \,. \tag{3.28}$$

The symbol "Pec" in these expressions is the cell Peclet number, which is the ratio of the convection flux to the diffusion flux. The Peclet number at the east face, Pec_e, is defined as

$$Pec_e = F_e / D_e \,. \tag{3.29}$$

The function C depends on the convection scheme used, and in this work the hybrid scheme is used. Then C takes the form

$$C(|Pec|) = \max\{0, 1-(½)|Pec|\}. \tag{3.30}$$

This scheme is essentially central difference for $|Pec_e| \leq 2$, and switches to first-order upwind for $|Pec_e| > 2$. For the problem under consideration, the source term is only linear in ϕ at most, and so for simplicity it is just lumped into the term B (Eq. (3.26)).

Special care should be taken in the discretization of boundary cells. As discussed before, there are only two kinds of boundary conditions involved: Dirichlet and Neumann. Figure 3.6 shows cell P with the south face being the boundary where the Dirichlet boundary condition is specified there, namely, ϕ_s is given. In this case, let point S coincide with point s, then

$$\phi_S = \phi_s . \tag{3.31}$$

Here also note the special definition of δy_s at the boundary cell, as could be seen clearly by comparing it with that in Fig. 3.5. With these two special definitions, the procedures and formulations to discretize the boundary cell are exactly the same as those for an interior cell as discussed before. By the same token, all other boundary cells, whether they are at the north or the east boundary, are discretized.

The Neumann boundary condition is treated in another way. Again, a cell P with the south face being the boundary where the $\partial\phi/\partial y$ is specified is taken as an example to demonstrate the boundary treatment. As shown in Fig. 3.7, an imaginary cell S is added to the south of cell P such that

$$\Delta y_S = \Delta y_P , \tag{3.32}$$

and so

$$\delta y_s = \Delta y_P . \tag{3.33}$$

Applying the boundary condition with central difference approximation yields

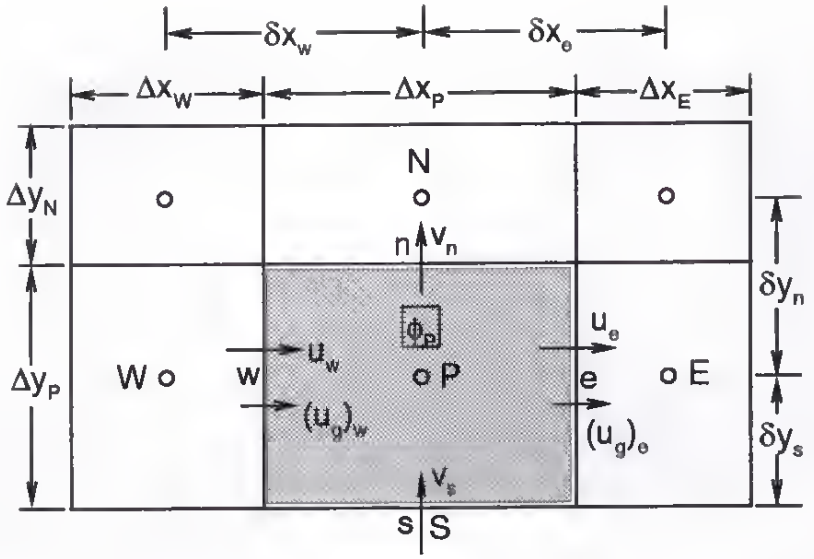

Fig. 3.6 A south boundary cell with Dirichlet boundary condition

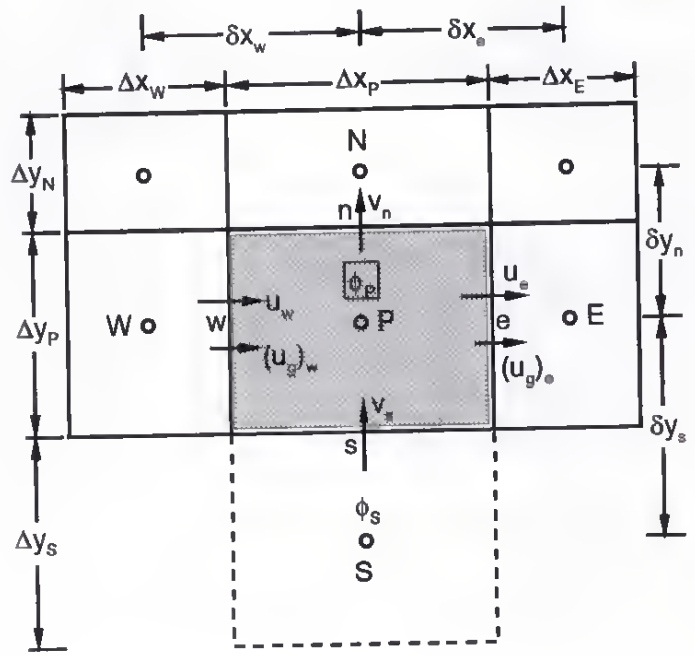

Fig. 3.7 A south boundary cell with Neumann boundary condition

$$(\frac{\partial \phi}{\partial y})_s = \frac{\phi_P - \phi_S}{\delta y_s} , \tag{3.34}$$

then,

$$\phi_S = \phi_P - (\frac{\partial \phi}{\partial y})_s \delta y_s . \tag{3.35}$$

Now the boundary cell P can be treated as if it were an interior cell. As mentioned in the last chapter, all the Neumann boundary conditions are with zero gradients in this study, consequently the last equation gives $\phi_S = \phi_s$ for such special cases.

Throughout the discretization process, linear interpolation is frequently used to evaluate values whenever they are not readily available, except ϕ's themselves at cell faces, which are determined by convection schemes instead. For instance, in evaluating the mass flux $F_n = \rho_n v_n \Delta x_P$ (refer to Fig. 3.7), if ρ_n is not readily available, as is the case when the control volume is for any quantity but v, then the density there should be approximated by linearly interpolating the values at the neighboring points.

It has been seen that the involvement of moving grids doesn't complicate the algorithm much. It is the velocity relative to the control surface that is used in defining the convection mass flux (refer to Eqs. (3.12) and (3.13)). Since the grid velocity in this work is neither zero nor the fluid velocity, the grid is neither Eulerian nor Lagrangian.

3.3 Solution Procedures

With the SIMPLE algorithm, the discretized governing equations are solved one at a time in a sequential manner. Besides, pressure is used as the basis, i.e., the

hydrodynamic pressure is determined by letting the velocity field satisfy the continuity equation, as is in contrast to the compressible algorithms (also called density-based algorithms) that use density as the basis by solving the density from the continuity equation and then determine pressure from the equation of state.

At the very beginning of the calculation, initial conditions must be properly specified. Then time is increased by Δt; at the new time level grids are generated based on the new boundaries and boundary conditions are specified accordingly. The flow and thermal fields need to be calculated, and the procedures are described as follows.

First, all the unknown quantities are guessed, and denoted as u^*, v^*, $(p^t)^*$, $(p^h)^*$, T^*, ρ^*, etc. Good initial guesses should correspond to the values at the last time level. With these guessed quantities, the u-momentum equation is discretized first. Since the way to discretize a general equation was already given in detail in the last section, only the final form of the discretized u-momentum equation for an u-control volume P is given here.

$$a_P u_P = \sum_{nb} a_{nb} u_{nb} - \Delta y_P (p_E^h - p_P^h) + s_u \ , \qquad (3.36)$$

where the source term is intentionally written into two parts such that the part solely related to the driving force--pressure--is separated from all other contributions, as this will help the discussion of pressure-velocity coupling.

Equation (3.36) is linearized already because the coefficients involved are evaluated in terms of the guessed u^* values but not the current u values. Every cell results in an equation like Eq. (3.36), and thus a system of linear algebraic equations for

u is formed, which is solved by an iterative method--the line successive relaxation method (Hirsch 1988). The u^* values can now be updated by the newly obtained u values,

$$u^* = \omega_u u^* + (1-\omega_u)u, \tag{3.37}$$

where ω_u is an underrelaxation parameter ($0<\omega_u<1$). Owing to the nonlinear coupling between the u-momentum equation and other equations, underrelaxation would be needed in updating u^* values so that the solution procedure converges.

The discretized v-momentum equation is given as

$$a_P v_P = \sum_{nb} a_{nb} v_{nb} - \Delta x_P (p_N^h - p_P^h) + s_v \ . \tag{3.38}$$

In a similar way, v is solved and v^* is updated with underrelaxation.

The velocity field determined this way, however, may not necessarily satisfy the continuity equation because the solution is based on a guessed hydrodynamic pressure field $(p^h)^*$. Therefore, the discretizing the continuity equation over a pressure-control volume at point P (refer to Fig. 3.5) yields

$$\frac{(\rho^* A)_P - (\rho A)_P^o}{\Delta t} + F_e^* - F_w^* + F_n^* - F_s^* = s_m^* \ (\neq 0) \ . \tag{3.39}$$

The pressure needs to be corrected so that the resultant velocity field satisfies the continuity equation. If the pressure correction is denoted by p′, then, from the momentum equations (3.36) and (3.38), the corresponding velocity corrections at the interfaces of the pressure-control volume are given by

$$u_e' = -\frac{\Delta y_P}{a_P}(p_E' - p_P') , \quad u_w' = -\frac{\Delta y_P}{a_P}(p_P' - p_W') , \tag{3.40}$$

and

$$v_n' = -\frac{\Delta x_P}{a_P}(p_N' - p_P') , \quad v_s' = -\frac{\Delta x_P}{a_P}(p_P' - p_S') . \tag{3.41}$$

Since there is a half-cell shift between the velocity- and pressure-control volumes, an index shift is also applied when deriving the above equations from the momentum equations. The coefficient a_p in Eqs. (3.40) differ from those in (3.41) because the u- and v-control volumes are not collocated. The corresponding flux corrections are

$$\begin{aligned}
F_e' &= \rho_e u'_e \Delta y_P = -\rho_e \frac{\Delta y_P}{a_P}(p_E' - p_P')\Delta y_P , \\
F_w' &= \rho_w u'_w \Delta y_P = -\rho_w \frac{\Delta y_P}{a_P}(p_P' - p_W')\Delta y_P , \\
F_n' &= \rho_n v'_n \Delta x_P = -\rho_n \frac{\Delta x_P}{a_P}(p_N' - p_P')\Delta x_P , \\
F_s' &= \rho_s v'_s \Delta x_P = -\rho_s \frac{\Delta x_P}{a_P}(p_P' - p_S')\Delta x_P .
\end{aligned} \tag{3.42}$$

It is required that the corrected pressure and velocity satisfy

$$\frac{(\rho^* A)_P - (\rho A)_P^o}{\Delta t} + F_e^* - F_w^* + F_n^* - F_s^* + F_e' - F_w' + F_n' - F_s' = 0 . \tag{3.43}$$

Substituting Eqs. (3.42) into Eq. (3.43) and collecting terms give the pressure correction equation

$$b_P p'_P = \sum_{nb} b_{nb} p'_{nb} - s^*_m , \tag{3.44}$$

where b's are the coefficients, and s^*_m is defined in Eq. (3.39). The latter quantity serves as a measure of how closely the continuity equation is satisfied.

It was mentioned in the last chapter that there are no explicit pressure boundary conditions for the problems under consideration. Pressure correction equations like Eq. (3.44), however, do need boundary conditions. Boundary conditions for p′ need to be derived from the given velocity boundary conditions. For example, consider a cell with the west face as the boundary where the normal velocity component, u, is predefined, then there should be no velocity (and therefore mass flux) correction there, i.e., F_w' in Eqs. (3.42) is zero. The F_w' term will not appear in Eq. (3.43), so the coefficient b_W in Eq. (3.44) takes the value of zero ($b_W = 0$).

After pressure corrections are solved from the pressure correction equation, the hydrodynamic pressure is updated by

$$p^h = (p^h)^* + \omega_p p', \tag{3.45}$$

where underrelaxation is used again to maintain convergence ($0<\omega_p<1$).

The corresponding velocity corrections u′ and v′ are calculated from Eqs. (3.40) and (3.41), respectively, and the velocity components are then updated as

$$u=u^*+u', \tag{3.46}$$

$$v=v^*+v'. \tag{3.47}$$

One should note that the energy equation is coupled with the continuity and momentum equations, and the reasons are 1) viscosity is a function of temperature, and

2) for the variable-density problem, density is also a function of temperature. So the discretized energy equation is solved with the guessed density ρ^* and the above updated velocity components. The thermodynamic pressure p^t can then be computed by using the method described in the last chapter via Eq. (2.23), and density is also updated from Eq. (2.21). Underrelaxation is also used in updating density.

With all the updated quantities, one goes back to the momentum equation again and repeats the solution procedures until the solutions are fully converged at the given time level. The time level is next increased by one when solutions have converged. Since the time-periodic problem is being simulated, it would take several cycles (or periods) for the numerical solution to reach a time-periodic state. Figure 3.8 gives a summary of the overall solution procedures in a flowchart.

3.4 Initial and Slow-Start Boundary Conditions

Because of the iterative feature of the solution procedure, good initial guesses for the unknown quantities can make the solution converge fast, as is especially the case at the very first time step. At t=0, the left piston velocity is zero (Eq. (2.24)), but the right piston velocity is not if $\varphi_o \neq 0$ (Eq. (2.25)). Meanwhile, if $T_c \neq T_h$, it would be difficult to specify the precise initial velocity and temperature conditions for the solution process to start with because the initial velocity and temperature fields are not uniform in such conditions. To circumvent such a difficulty, a slow-start procedure was utilized in specifying temperature boundary conditions, and the phase angle lag φ, and therefore the velocity boundary conditions as well.

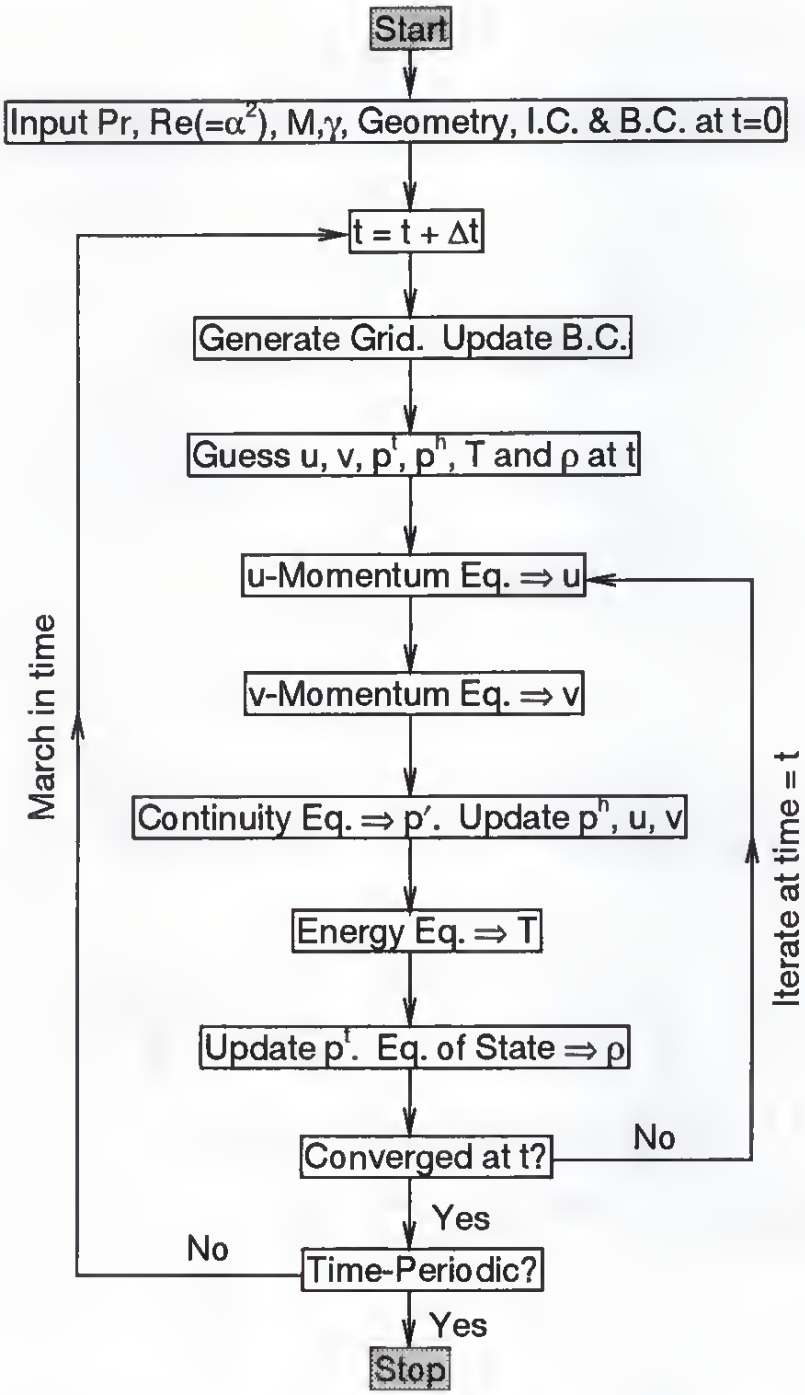

Fig. 3.8 Solution procedures for variable-density time-periodic flow and heat transfer problems

A quantity φ is defined by the following expression,

$$\varphi = \begin{cases} \frac{\varphi_o}{2}[1-\cos(2\omega t)] , & 0 \le \omega t < \frac{\pi}{2} , \\ \varphi_o , & \frac{\pi}{2} \le \omega t , \end{cases} \tag{3.48}$$

where φ_o is the desirable phase angle. The newly defined φ will take the place of φ_o in the expression for x_{right} in Figs. 1.3 and 1.4, and also in Eq. (2.25) for u_{right}. Then at t=0, both pistons have zero velocity, and so the velocity in the whole computational domain is also zero. It takes a quarter of the first cycle for φ to adjust smoothly to its final value φ_o.

For temperature boundary conditions, suppose that the desirable chamber wall temperatures are: T_c for the left chamber and T_h for the right, then define

$$T_{left} = \begin{cases} \frac{1}{2}\{(T_h+T_c) - \frac{(T_h-T_c)}{2}[1-\cos(2\omega t)]\} , & 0 \le \omega t < \frac{\pi}{2} , \\ T_c , & \frac{\pi}{2} \le \omega t , \end{cases} \tag{3.49}$$

and

$$T_{right} = \begin{cases} \frac{1}{2}\{(T_h+T_c) + \frac{(T_h-T_c)}{2}[1-\cos(2\omega t)]\} , & 0 \le \omega t < \frac{\pi}{2} , \\ T_h , & \frac{\pi}{2} \le \omega t , \end{cases} \tag{3.50}$$

where T_{left} and T_{right} are the temperatures to be specified as the boundary conditions for the corresponding chamber walls. At t=0, $T_{left}=T_{right}$, hence a uniform initial

temperature field is expected. Over a quarter of the first cycle, the boundary temperatures gradually develop to the desirable values.

3.5 Code Validation

The proposed pressure-splitting method and the code developed were validated for variable-density, time-periodic flows and heat transfer in regions with moving boundaries. The first test case is a 2D piston-cylinder set-up with all the boundaries being insulated (Fig. 3.9). Air is present in the cylinder with initial pressure $p_o=1$ std atm ($=1.013\text{x}10^5$ N/m^2), temperature $T_o=288.15$ K, and density $\rho_o=1.225$ kg/m^3. At the very beginning, the piston stands still at $x=0$, so there is no fluid motion. Then the piston oscillates, and its location is given by

$$x_{piston} = \begin{cases} \frac{\varepsilon}{2}[\cos(\omega t) - 1], & 0 \le \omega t < \pi, \\ \varepsilon\cos(\omega t), & \pi \le \omega t. \end{cases} \tag{3.51}$$

The oscillation frequency is $f=1$ Hz ($\omega=2\pi f=2\pi$ rad/s). The geometric parameters are $a=1\text{x}10^{-3}$ m, $\varepsilon=1a$, and $L=3a$. The nondimensional parameters are $\gamma=1.4$, $Pr=0.72$, $\alpha=0.6559$ and $M=1.846\text{x}10^{-5}$. It is known from thermodynamics that for such small dimensions and slow oscillations the thermodynamic quantities should be uniform within the cylinder, and the quantities can be determined analytically by the adiabatic relationships:

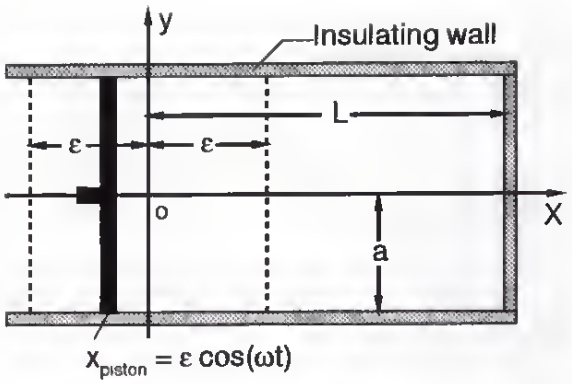

Fig. 3.9 A piston-cylinder set-up

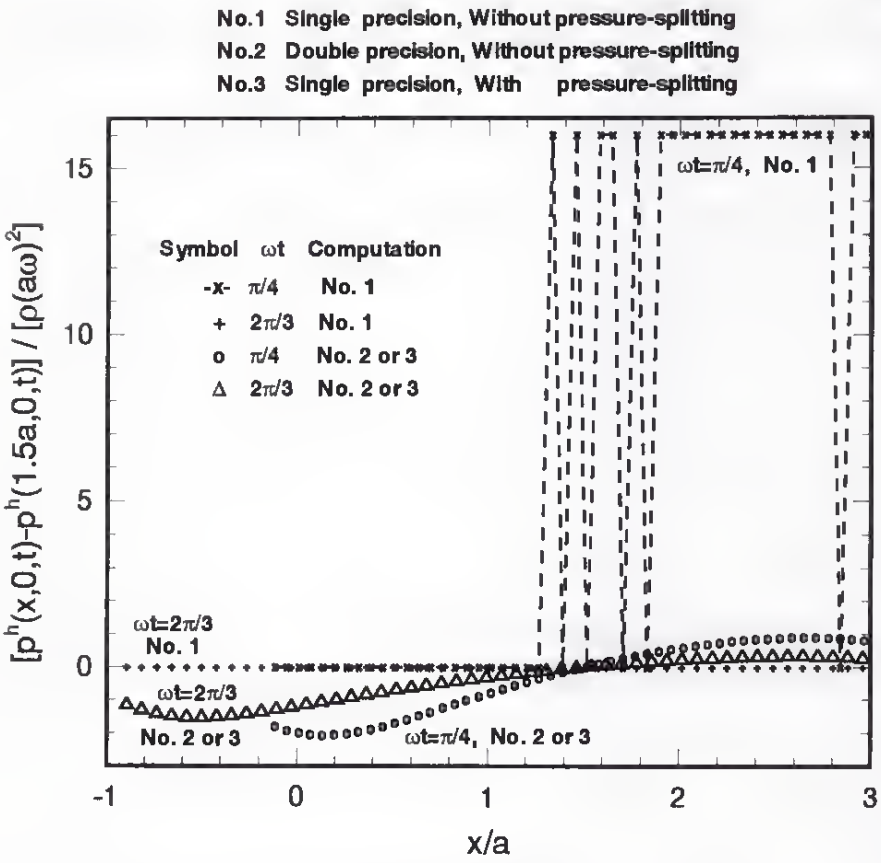

Fig. 3.10 Computed hydrodynamic pressure distributions along the x axis for the piston-cylinder set-up

$$\frac{p^t}{p_o^t} = \left(\frac{\forall_o}{\forall}\right)^\gamma = \left(\frac{\rho}{\rho_o}\right)^\gamma = \left(\frac{T}{T_o}\right)^{\frac{\gamma}{\gamma-1}}, \qquad (3.52)$$

where $\forall$ is the total volume and the subscript "o" denotes initial values.

This case was computed numerically on a machine with significant digits of seven for single precision and of 16 for double precision. It was first computed with single precision and without split pressures (denoted as Computation No. 1), next it was computed with double precision and still without split pressures (Computation No. 2), and finally the same case was computed with single precision and with split pressures (Computation No. 3). The numerical pressure distributions along the x axis are plotted against each other in Fig. 3.10. The pressure shown in the figure is actually the pressure difference with respect to the point (x,y)=(1.5a,0), therefore the pressure is the hydrodynamic pressure p^h. As indicated by the figure, at time $\omega t=\pi/4$, the hydrodynamic pressure from Computation No. 1 oscillates wildly along the x axis, but at $\omega t=2\pi/3$, it is just uniform. None of these two distributions is physically realistic. When the computation accuracy is increased by using double precision (Computation No. 2), the hydrodynamic pressure distribution is neither oscillating nor uniform. Such an observation reveals that for problems like this, the pressure field cannot be correctly resolved by using the computational algorithm of Computation No. 1, and using double precision in the calculations (Computation No. 2) is indeed one remedy. Figure 3.10 clearly shows that Computation No. 3 yields the same pressure as Computation No. 2 does. Since Computation No. 3 uses single precision, it saves computer CPU time by about 30%, memory and storage by almost 50% over Computation No. 2. This proves

the significant benefits given by using the pressure-splitting algorithm, and verifies the analysis presented in the last chapter.

The instantaneous thermodynamic pressure, $p^t(t)$, in the third oscillation cycle is shown in Fig. 3.11. To help compare the magnitudes of p^h and p^t, p^t in this figure is normalized with the same quantity as that for p^h. By comparing Figs. 3.10 and 3.11, it can be seen that the magnitude of the thermodynamic pressure is greater than that of the hydrodynamic pressure by nine orders. It is for this reason that Computation No.1 with only seven significant digits can not accurately resolve the pressure field when the thermodynamic and hydrodynamic pressures are not treated separately in the solution.

In Fig. 3.12, the numerical temperature distribution along the x axis is plotted against the analytical solution. At a given time, the analytical temperature distribution is uniform, as is presented by the horizontal line in the figure. The temperature from Computation No. 1 is not uniform, but varies along the x axis. The incorrect temperature is produced by the erroneous velocity field resulting from the pressure field that is not accurately resolved numerically. It can also be seen that the numerical temperature distribution either from Computation No. 2 or from Computation No. 3 is in perfect agreement with the analytical solution, which again shows that the proposed pressure-splitting technique not only gives the right solutions, but also saves computer CPU time, memory and storage substantially.

In the second test case, the set-up is similar to Model A1 except that the piston surfaces are isothermal. Geometric parameters are (refer to Fig. 1.3a): $a=1\times10^{-3}$ m, $b=4a$, $c=3a$, $\varepsilon=2a$ and $L=6a$. The wall temperature (including the piston's) is kept at

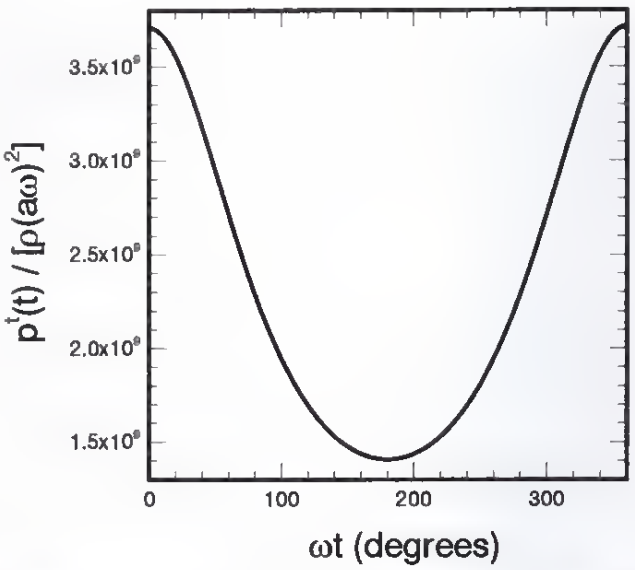

Fig. 3.11 Thermodynamic pressure in the third cycle for the piston-cylinder set-up

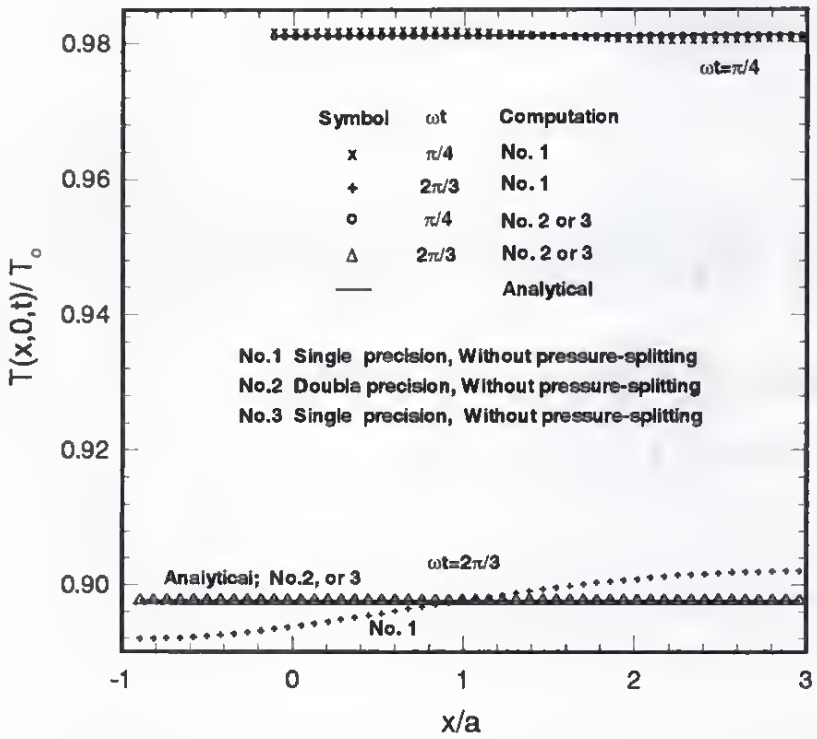

Fig. 3.12 Temperature distributions along the x axis for the piston-cylinder set-up

constant T_w=288.15 K (therefore T_c=T_h=T_w). Pistons oscillate sinusoidally with the right piston leading the left by 90° in phase (φ_o=90°) with an oscillation frequency of f=2.32 Hz. Air is the working medium. At t=0, p_o=1 atm, T_o= 288.15 K, ρ_o=1.225 kg/m^3. The corresponding nondimensional parameters are γ=1.4, Pr=0.72, α=1 and M=4.29x10^{-5}.

In this calculation, the pressure-splitting algorithm is used. For the computational domain, which is only the upper half geometry, a 91x31 grid system is used. The grid distribution is: 31x31 in the left chamber, 31x11 in the channel, and 31x31 in the right chamber. The time step is chosen such that each cycle is discretized into 360 uniform intervals, i.e., $\Delta t = 1/(360f) = 1.2\text{x}10^{-3}$ sec. It takes about four cycles for the solution to reach the time-periodic state.

The P-V diagram for this calculation is shown in Fig. 3.13. This figure shows that the minimum pressure is p_{min}/p_o=0.7099 and the maximum is p_{max}/p_o=1.6420, which can be checked by examining two extreme conditions, namely isothermal and adiabatic. For an isothermal condition,

$$p/p_o = \forall_o/\forall \ ,$$

so, $$p_{min}/p_o = \forall_o/\forall_{max} = 0.7262, \text{ and } p_{max}/p_o = \forall_o/\forall_{min} = 1.6055.$$

For an adiabatic condition,

$$p/p_o = (\forall_o/\forall)^\gamma,$$

so, $$p_{min}/p_o = (\forall_o/\forall_{max})^\gamma = 0.6389, \text{ and } p_{max}/p_o = (\forall_o/\forall_{min})^\gamma = 1.9402.$$

The numerical maximum should be larger than the adiabatic counterpart and less than the isothermal one, whereas the numerical minimum should be larger than the isothermal one

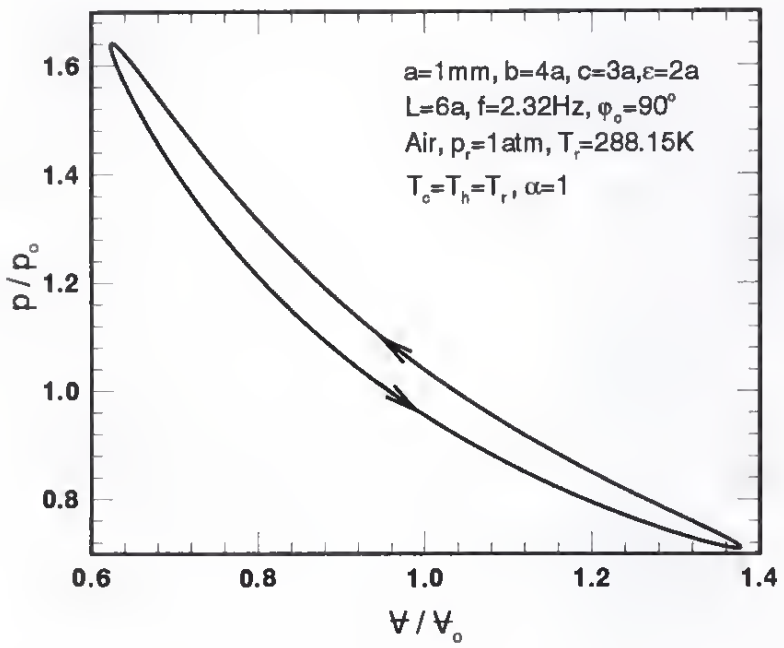

Fig. 3.13 P-V diagram of the second test case

and less than the adiabatic one; moreover, numerical values should be closer to the isothermal values than to the adiabatic ones because of the boundary condition of isothermal walls. That is indeed the case:

minimum: 0.6389 (adiabatic) < 0.7099 (numerical) < 0.7262 (isothermal),

maximum: 1.6035 (isothermal) < 1.6420 (numerical) < 1.9402 (adiabatic).

The correctness of the numerical solution is also supported by checking the overall energy balance. First define the power input--the mean rate at which work is done on the gas by some external force--as

$$P = \frac{1}{\tau} \int_0^{\tau} \{ \int_{\forall(t)} -p d\forall \} dt \ , \tag{3.53}$$

where τ is the period of piston oscillations, i.e. $\tau = 2\pi/\omega$.

The mean rate at which heat is transferred out of some domain is

$$Q = \frac{1}{\tau} \int_0^{\tau} \{ \int_{S_{wet}(t)} -k \nabla T \cdot \hat{n} dS \} dt \ , \tag{3.54}$$

where $S_{wet}(t)$ represents the solid surface that is in contact with the gas, and the surface may change with time.

The rate at which the gas "absorbs" heat through the left chamber walls plus the piston surface is Q_{left}=2.4589D watts (here D is the depth in the third dimension in meters); the rate at which heat is rejected out of the gas through the channel walls is $Q_{channel}$=0.5516D watts, and that through the right chamber walls plus the piston surface is Q_{right}=2.7297D watts. The power input is P=0.8415D watts. According to the first law of thermodynamics, the following expression holds,

$$Q_{left} - Q_{channel} - Q_{right} = -P.$$

Then, LHS = 2.4589 - 0.5516 - 2.7297 = -0.8224,

RHS = -0.8415.

Therefore, there is only a very small relative error of 2.3% in the total energy balance.

The preceding two test cases have verified that the pressure-splitting algorithm is computationally accurate and efficient, and in the mean time they have also validated the computer code.

CHAPTER 4
RESULTS AND DISCUSSION

By using this code, investigations were made on the models' cooling capacity and efficiency in terms of working gases, oscillation frequencies, channel length, ratios of the chamber width to the channel width, etc. The velocity and temperature fields were also examined. Discussion is made on the criterion for the model to result in good regeneration. Table 4.1 lists the cases that were studied. Note that to make the number of parameters appearing in the table as small as possible, yet adequate to present each case, those parameters that can be obtained directly, or via auxiliary relations if needed, are omitted there. For instance, parameters that do not need such relations are: the ratio of specific heats ($\gamma=1.4$ for air and $\gamma=1.7$ for helium), Prandtl number ($Pr=0.72$ for air and $Pr=0.67$ for helium), and the constant T_μ used in the Southerland's formula (Eq. (3.9)) ($T_\mu=110.4$ K for air and $T_\mu=61.67$ K for helium). One of the parameters that need such relations is the reference density ρ_r, which can be obtained via the equation of state as $\rho_r=p_r/(RT_r)$ with R being 287 J/(Kg·K) for air and 2077.2 J/(Kg·K) for helium. For the meanings of the geometric parameters listed in Table 4.1, please refer to Figs. 1.3 and 1.4.

Tabel 4.1 List of the cases investigated

Case No.	Model	a [m] x10^3	l_s/a	c/a	d/a	ε/a	L/a	φ_o [°]	Gas	p_r [atm]	T_r [K]	T_c/T_r	T_h/T_r	f [Hz]	α	M x10^6
1	B1	1	6	8	N/A*	7	12	90	Helium	1	288.2	0.9	1.1	1	0.229	6.291
2	A1	1	6	8	N/A	7	24	90	Helium	1	288.2	0.9	1.1	1	0.229	6.291
3	A2	1	6	8	6	7	24	90	Helium	1	288.2	0.9	1.1	1	0.229	6.291
4	B2	1	6	8	6	7	24	90	Helium	1	288.2	0.9	1.1	1	0.229	6.291
5	B2	1	6	8	6	7	24	90	Air	1	288.2	0.9	1.1	1	0.656	18.46
6	A1	1	6	8	N/A	8	10	45	Helium	1	288.2	0.9	1.1	1	0.229	6.291
7	A1	1	6	8	N/A	2	10	75	Helium	1	288.2	0.9	1.1	1	0.229	6.291
8	A1	1	6	8	N/A	2	10	90	Helium	1	288.2	0.9	1.1	1	0.229	6.291
9	A1	1	6	8	N/A	2	10	105	Helium	1	288.2	0.9	1.1	1	0.229	6.291
10	A1	1	6	3	N/A	8	10	135	Helium	1	288.2	0.9	1.1	1	0.229	6.291
11	A1	1	6	8	N/A	2	10	90	Helium	1	288.2	0.95	1.05	1	0.229	6.291
12	A1	1	6	8	N/A	2	10	90	Helium	1	288.2	0.85	1.15	1	0.229	6.291
13	A1	1	6	8	N/A	2	10	90	Helium	1	288.2	0.8	1.2	1	0.229	6.291
14	A1	1	6	3	N/A	8	10	90	Helium	1	288.2	0.7716	1.2284	1	0.229	6.291
15	A1	1	6	3	N/A	2	10	90	helium	1	288.2	0.75	1.25	1	0.229	6.291
16	A1	1	6	8	N/A	7	12	90	Helium	1	288.2	0.9	1.1	1	0.229	6.291
17	B1	1	6	8	N/A	7	12	90	Helium	1	288.2	0.9	1.1	1	0.229	6.291

* N/A denotes not applicable for the case.

Table 4.1--Continued

Case No.	Model	a [m] x10^3	b/a	c/a	d/a	ε/a	L/a	φ_o [°]	Gas	p_r [atm]	T_r [K]	T_e/T_r	T_e/T_r	f [Hz]	α	M x10^6
18	B1	1	12	8	N/A	7	12	90	Helium	1	288.2	0.9	1.1	1	0.229	6.291
19	B1	1	15	8	N/A	7	12	90	Helium	1	288.2	0.9	1.1	1	0.229	6.291
20	A1	1	6	3	N/A	2	10	90	Helium	1	288.2	0.9	1.1	10	0.724	62.91

4.1 Velocity and Thermodynamic Fields of a Typical Case

In this section, the computations and results of Case 1 (refer to Table 4.1) are examined. Computations were made on the Cray C90 supercomputer of the Pittsburgh Supercomputer Center. Different grids and time step sizes were first tested to make sure that they were fine enough for the numerical solutions to be accurate enough. It was identified that for this particular case a reasonable choice was: a grid system of 2153 points (31x31 in the left chamber, 21x11 in the channel, and 31x31 in the right channel) and a time step size of $\Delta t = \tau/360$ ($= 2.78 \times 10^{-3}$ sec.), for further refining either the grid or the time step size did not result in any noticeable changes in the numerical solutions. The grids at $\omega t = \pi/4$ and $\omega t = \pi$ for this case can also be found in Figs. 3.1 (a) and (b) respectively, though these figures originally served another purpose there. Solution iteration numbers used were: 8 iterations for solving the u-momentum equation, 8 for the v-momentum equation, 40 for the p' equation and 8 for the energy equation; and 300 repetitions of the above procedures at a give time level. Under these given conditions, it took about 5472 second CPU time to run one cycle on the Cray C90 machine.

Figures 4.1 (a) and (b) plot the transient processes of the thermodynamic pressure and the pressure drop between the left and right pistons. These figures reflect the slow-start velocity and temperature conditions in the initial quarter cycle discussed at the end of the last chapter. Figure 4.1 (b) shows that the (hydrodynamic) pressure drop adjusts itself to time-periodic state only in few cycles. The thermodynamic pressure oscillates in the range of 0.5 to 2.5 atms, whereas the hydrodynamic pressure drop is only in the range of -2×10^{-6} to 2×10^{-6} atms, with the latter being only about one millionth of the

(a) Thermodynamic pressure

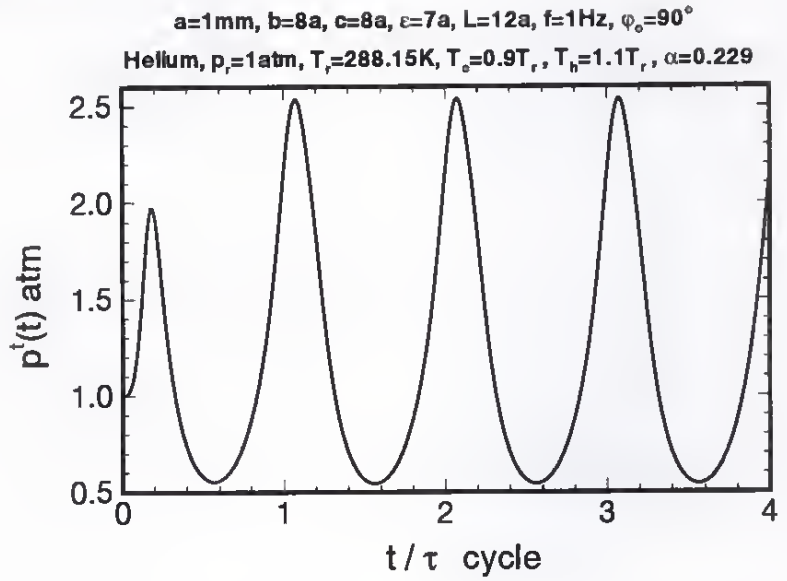

(b) Pressure drop

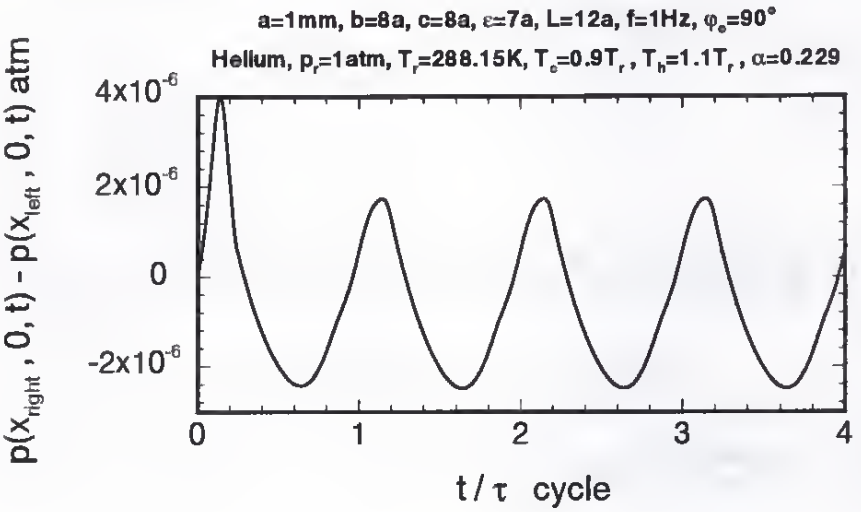

Fig. 4.1 Transient processes of pressures.
(a) Thermodynamic pressure; (b) Pressure drop between pistons.

former.

A way to check if numerical solutions have reached the time-periodic state is to compare the current solutions with those at the time one cycle earlier. The quantity σ defined below is such a measure.

$$\sigma_\phi = \frac{\sum_{ij} |\phi_{ij}^t - \phi_{ij}^{t-\tau}|}{\sum_{ij} \frac{1}{2}\{|\phi_{ij}^t| + |\phi_{ij}^{t-\tau}|\}}, \qquad (4.1)$$

where ϕ is a general notation representing any specific dependent variable of u, v, p^h, T or ρ. Such a measure is objective, because it takes the overall domain into account by the summation and meanwhile is a relative measure by adding the denominator in the definition. Figure 4.2 plots the quantities σ_u, σ_v, σ_{ph} and σ_T in the logarithmic scale vs. time. At any given time, they are of the same order and they all decrease linearly as time increases. The lines of $\log\sigma_\phi$'s have exactly the same slope.

Figures 4.3 (a), (b), (c) and (d) give the velocity vectors at time instants $\omega t=0$, $\pi/2$, π and $3\pi/2$, respectively. Note that to have a better view of the field quantity in the configuration, the domain shown in the figures is actually as large as six times the computational domain. No significant circulation region is observed for this case because of the small Womersley number used.

The corresponding hydrodynamic pressure contours are plotted in Figs. 4.4 (a), (b), (c) and (d). These figures show that when neither piston is extremely close to the channel exit, pressure drops mainly occur in the channels, otherwise the pressure drop in the transverse direction within the chamber is comparable to that in the channel. The

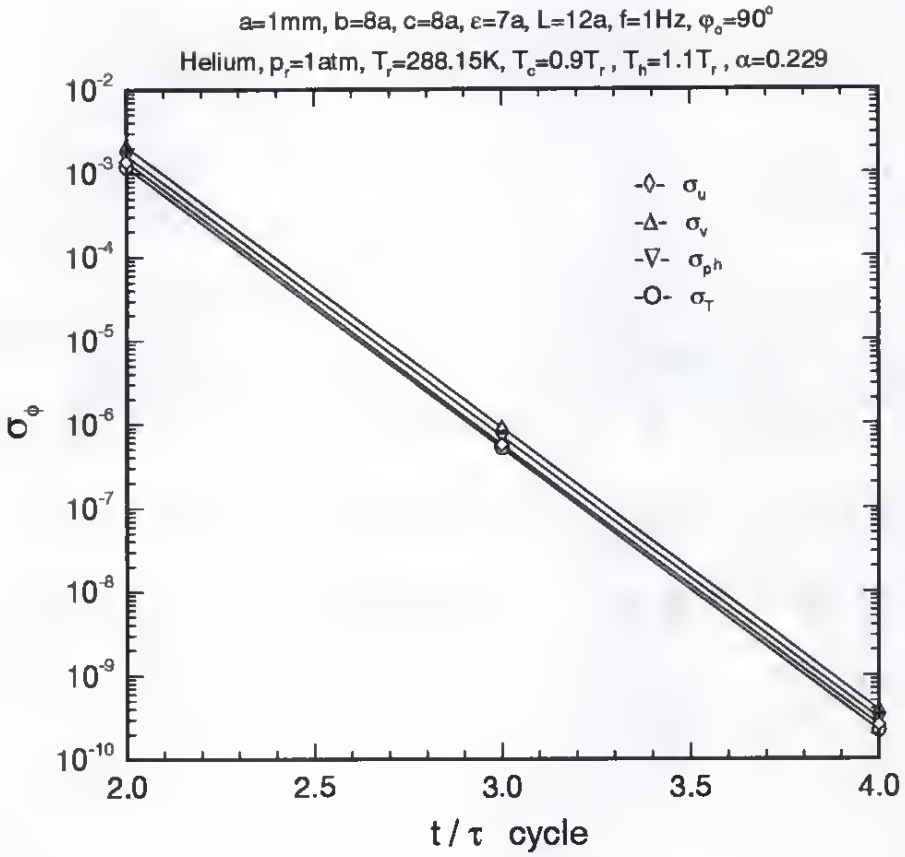

Fig. 4.2 Convergence history to time-periodic state

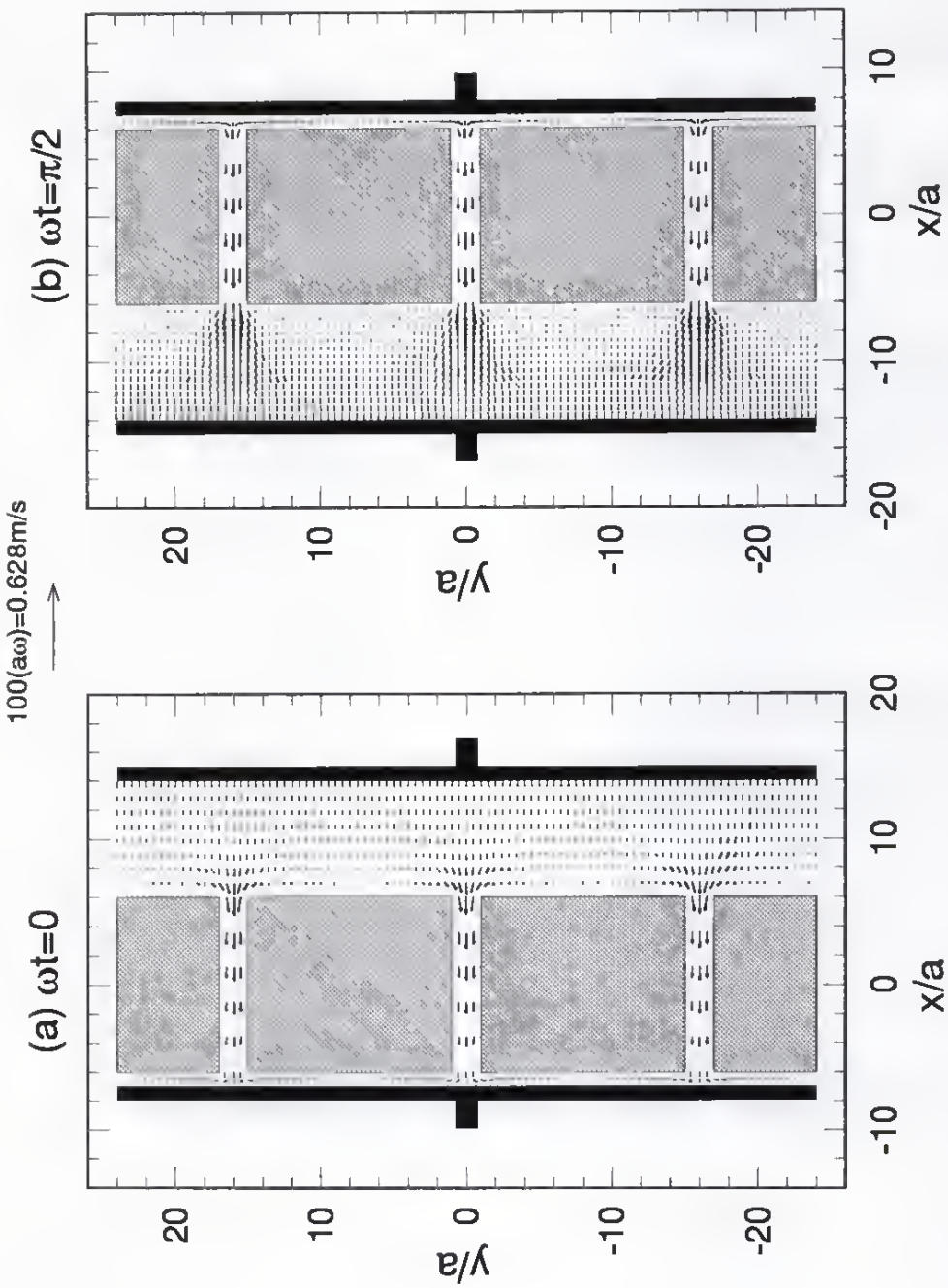

Fig. 4.3 Velocity fields of Case 1. (a) $\omega t=0$; (b) $\omega t=\pi/2$; (c) $\omega t=\pi$; (d) $\omega t=3\pi/2$.

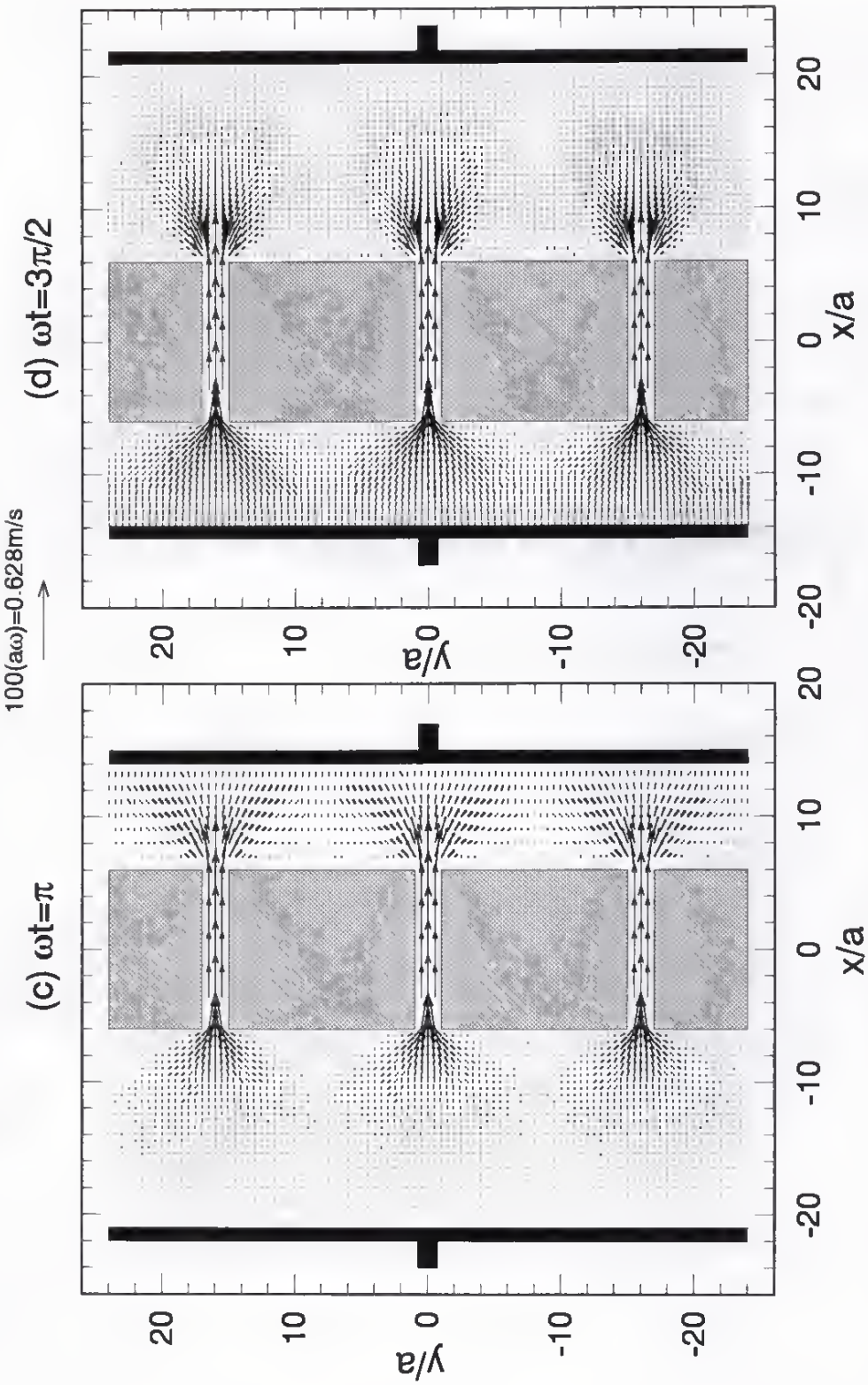

Fig. 4.3--continued

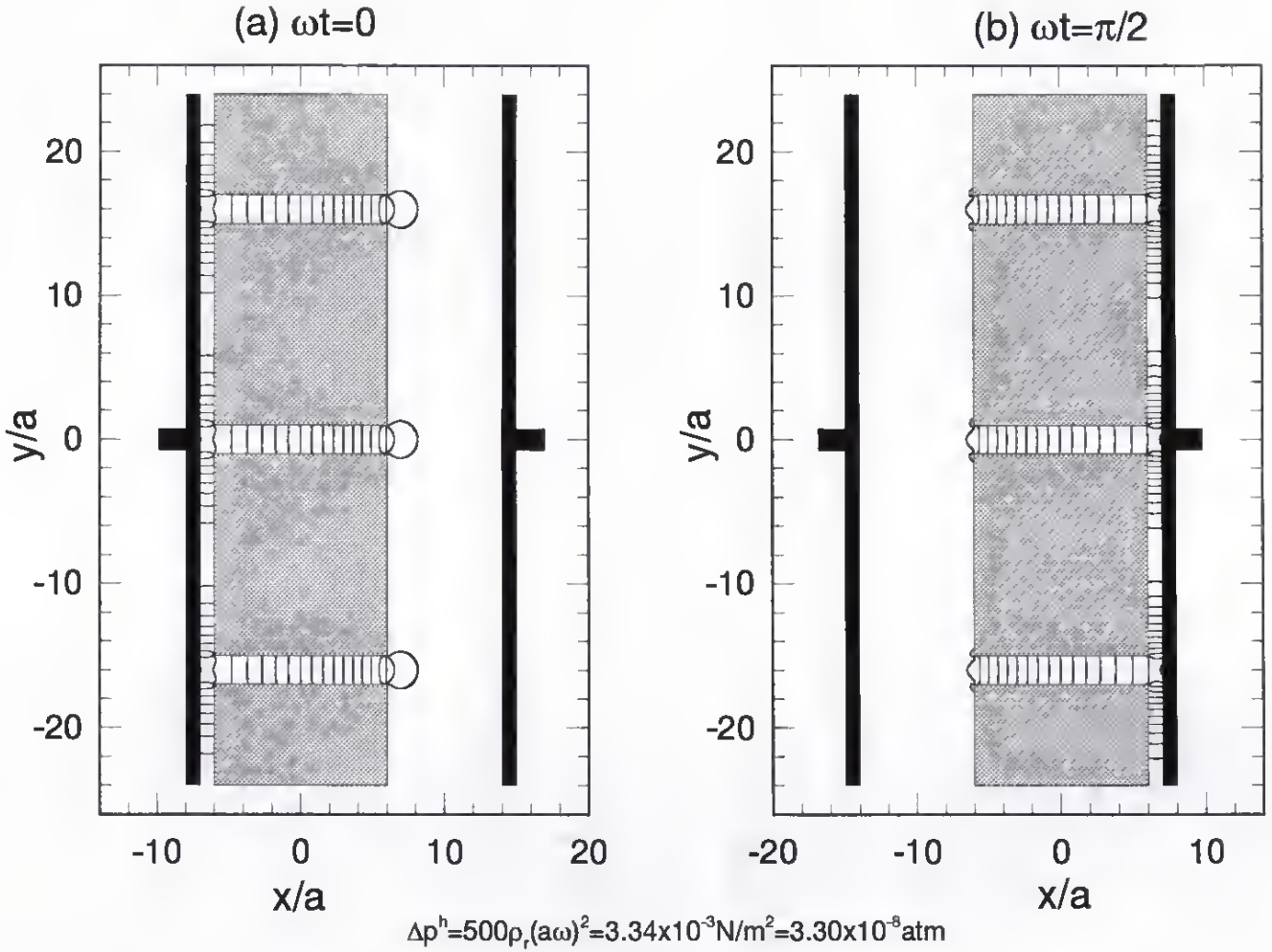

Fig. 4.4 Hydrodynamic pressure contours of Case 1. (a) $\omega t=0$; (b) $\omega t=\pi/2$; (c) $\omega t=\pi$; (d) $\omega t=3\pi/2$.

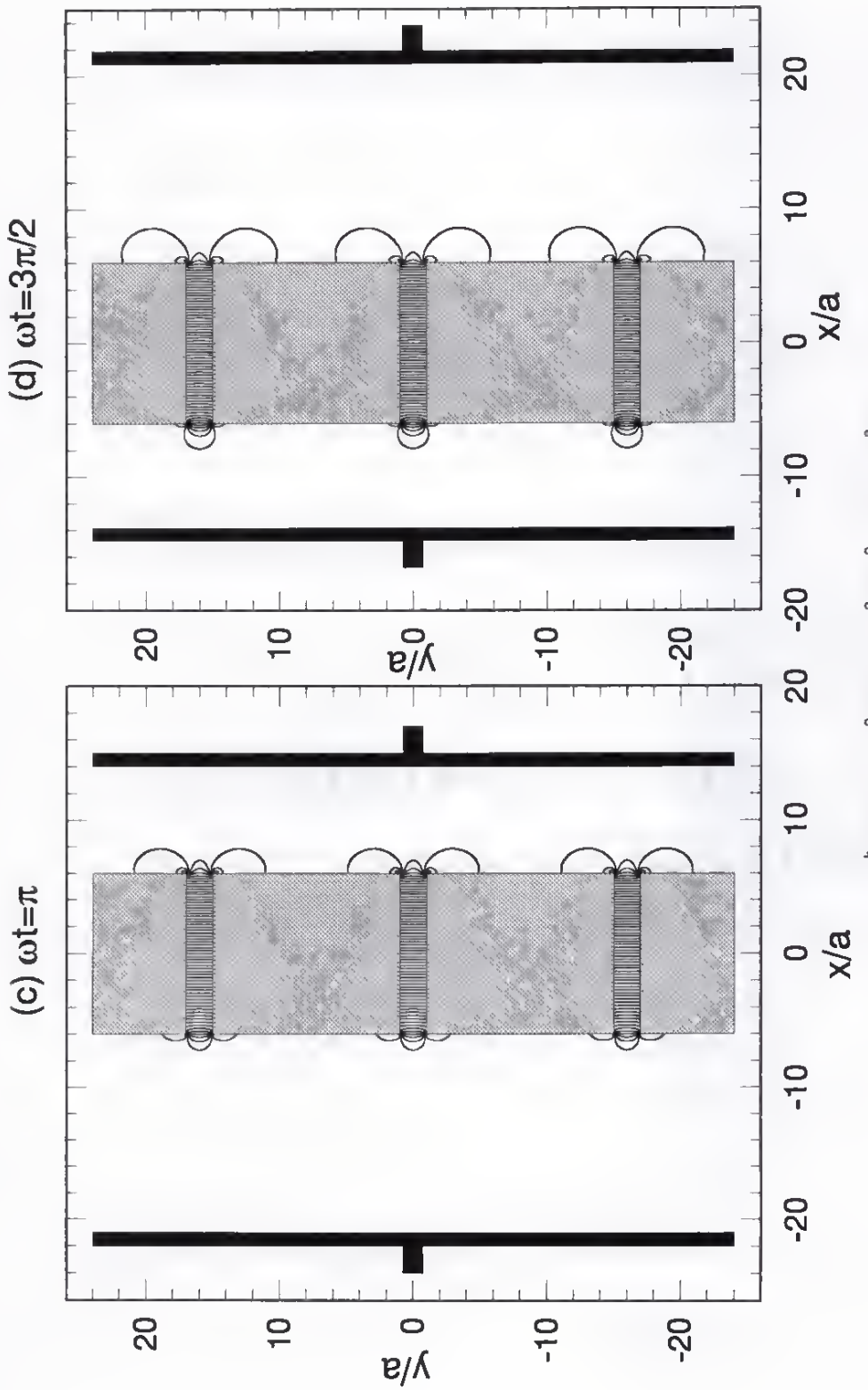

Fig. 4.4--continued

total pressure drop in space is only a few millionths of an atmosphere at most. It will be seen later that this is in contrast with the thermodynamic pressure, which changes with time by an amount in the order of one atmosphere.

Figures 4.5 (a), (b), (c) and (d) demonstrate the temperature contours. At all the times, the temperature of the gas within the channel is very close to the local channel wall temperature, indicating that the channel functions as a regenerator properly. At $\omega t=0$ (Fig. 4.5 (a)), which is at the compression stage, the temperature in the right chamber is much higher than that of the right chamber wall (1.1 nondimensional), and a value as high as 1.625 is observed. Inversely, at $\omega t=\pi$ (Fig. 4.5 (c)), which is at the expansion stage, the temperature in the left chamber is much lower than that of the left chamber wall (0.9), and a value of 0.625 is observed there. On average over time and space the mean gas temperature in the right chamber is higher than that of the chamber wall, so heat is rejected out of the gas through the right chamber wall; on the other hand, the mean gas temperature in the left chamber is lower than that of the chamber wall, and heat is absorbed by the gas there.

Density contours, shown in Fig. 4.6 (a), (b), (c) and (d), indicate that density changes significantly with time and space. For the time instants chosen, the nondimensional density takes values from 0.55 to 2.4. At any time, the patterns of density contours look like those of temperature contours due to the reciprocal relationship between density and temperature at a given time (Eq. (3.9)).

Figure 4.7 plots the P-V diagram for this case. The direction of the loop is counterclockwise, indicating that some external force does work on the gas. The power

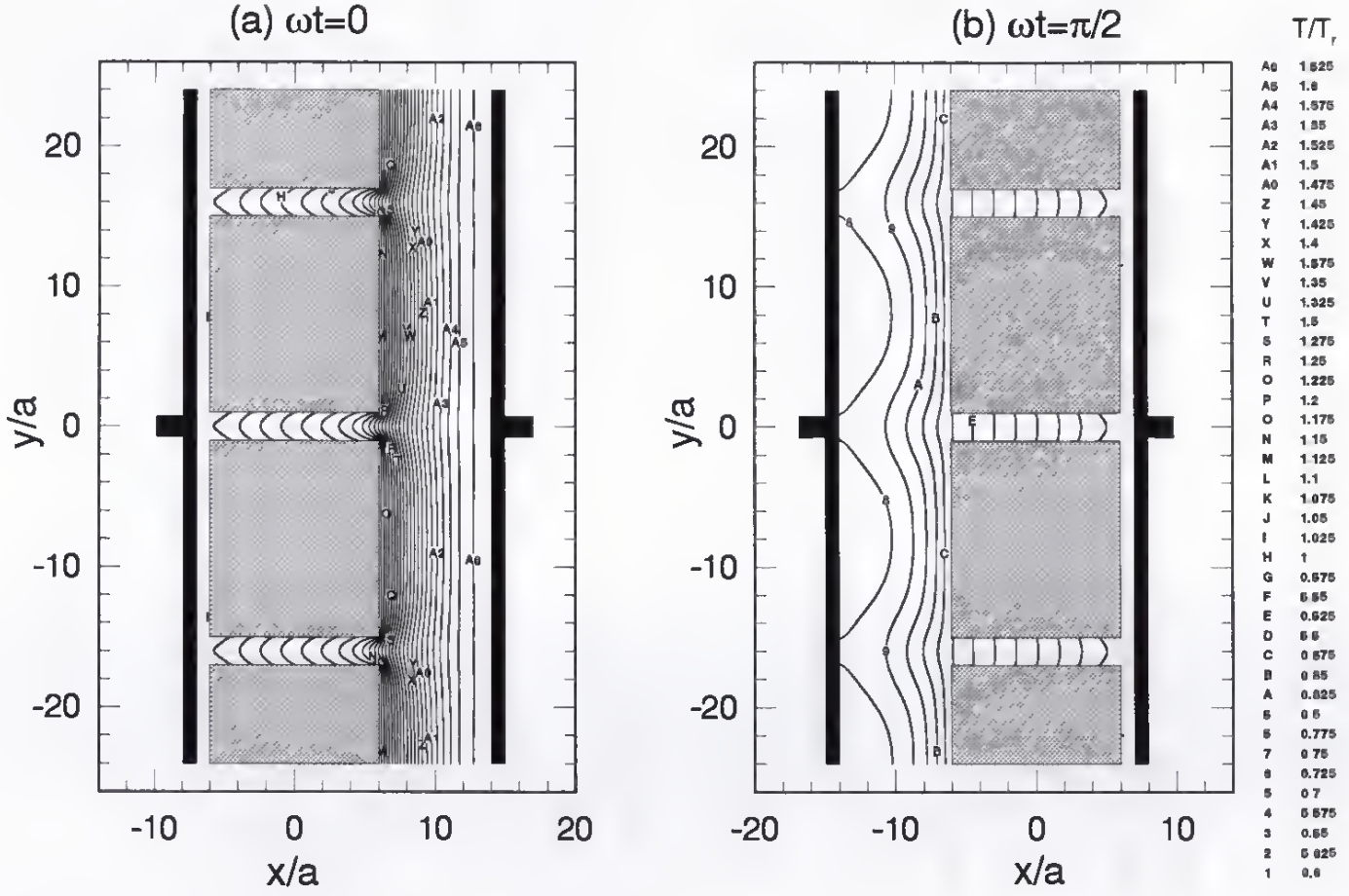

Fig. 4.5 Temperature contours of Case 1. (a) $\omega t=0$; (b) $\omega t=\pi/2$; (c) $\omega t=\pi$; (d) $\omega t=3\pi/2$.

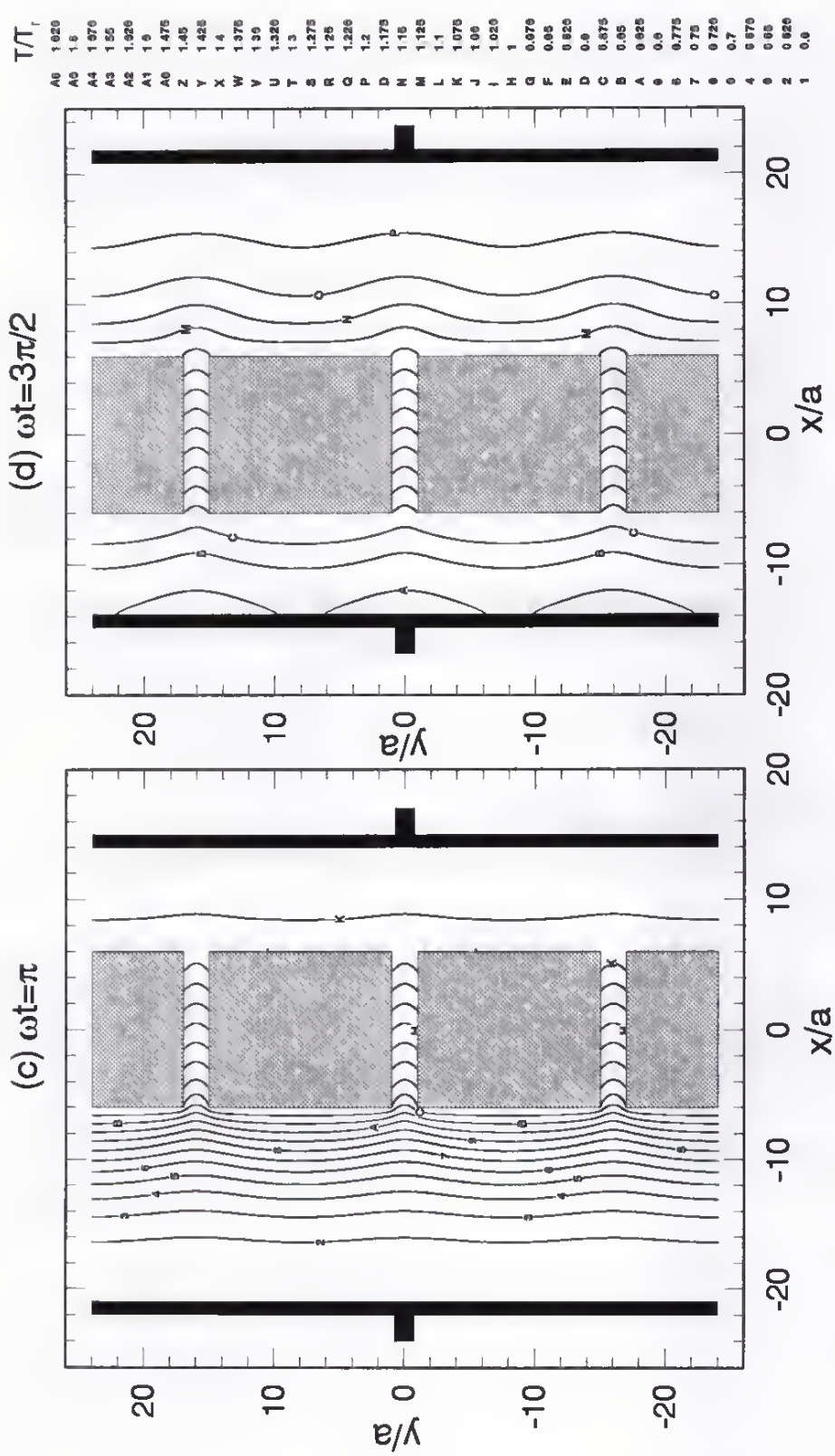

Fig. 4.5--continued

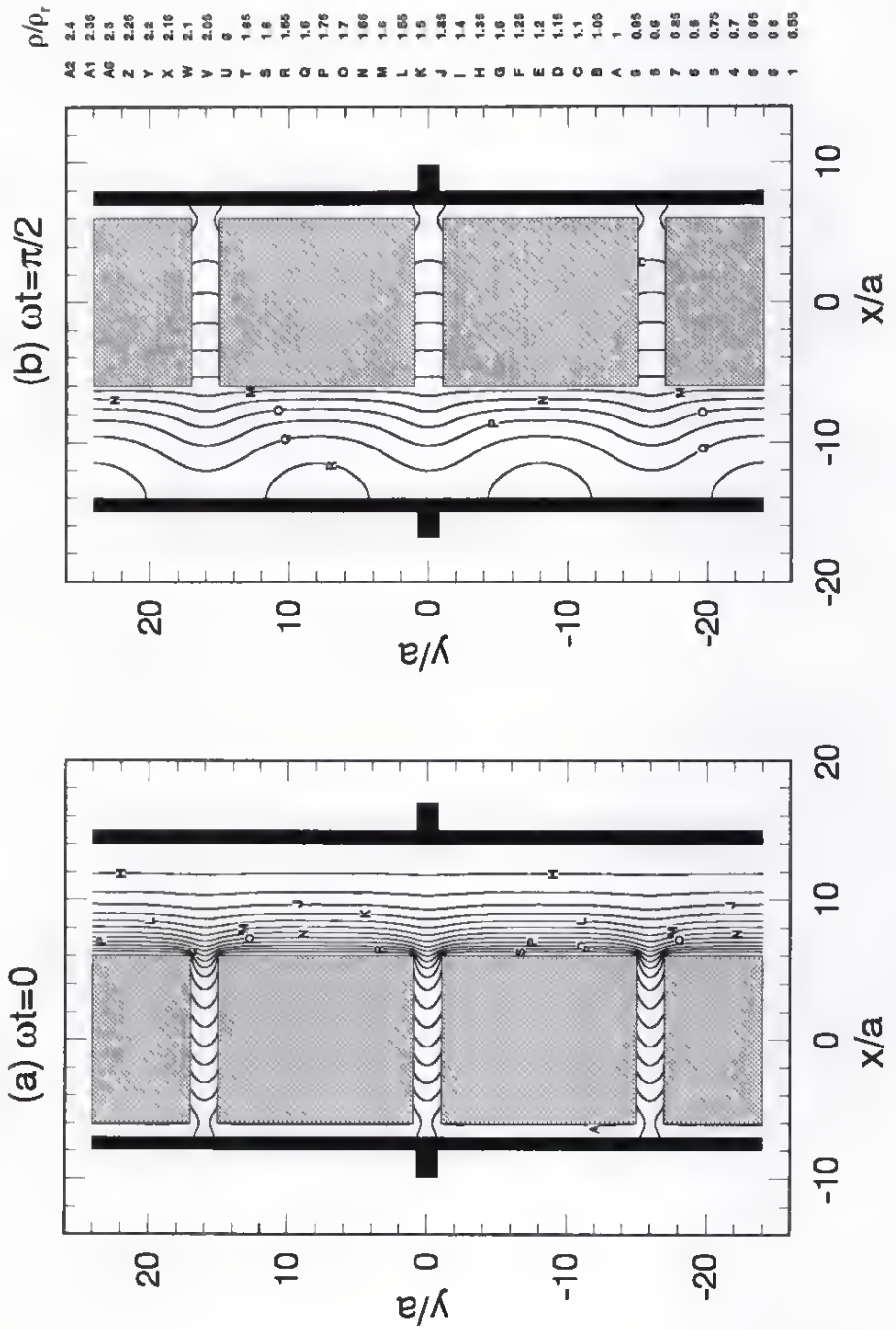

Fig. 4.6 Density contours of Case 1. (a) $\omega t=0$; (b) $\omega t=\pi/2$; (c) $\omega t=\pi$; (d) $\omega t=3\pi/2$.

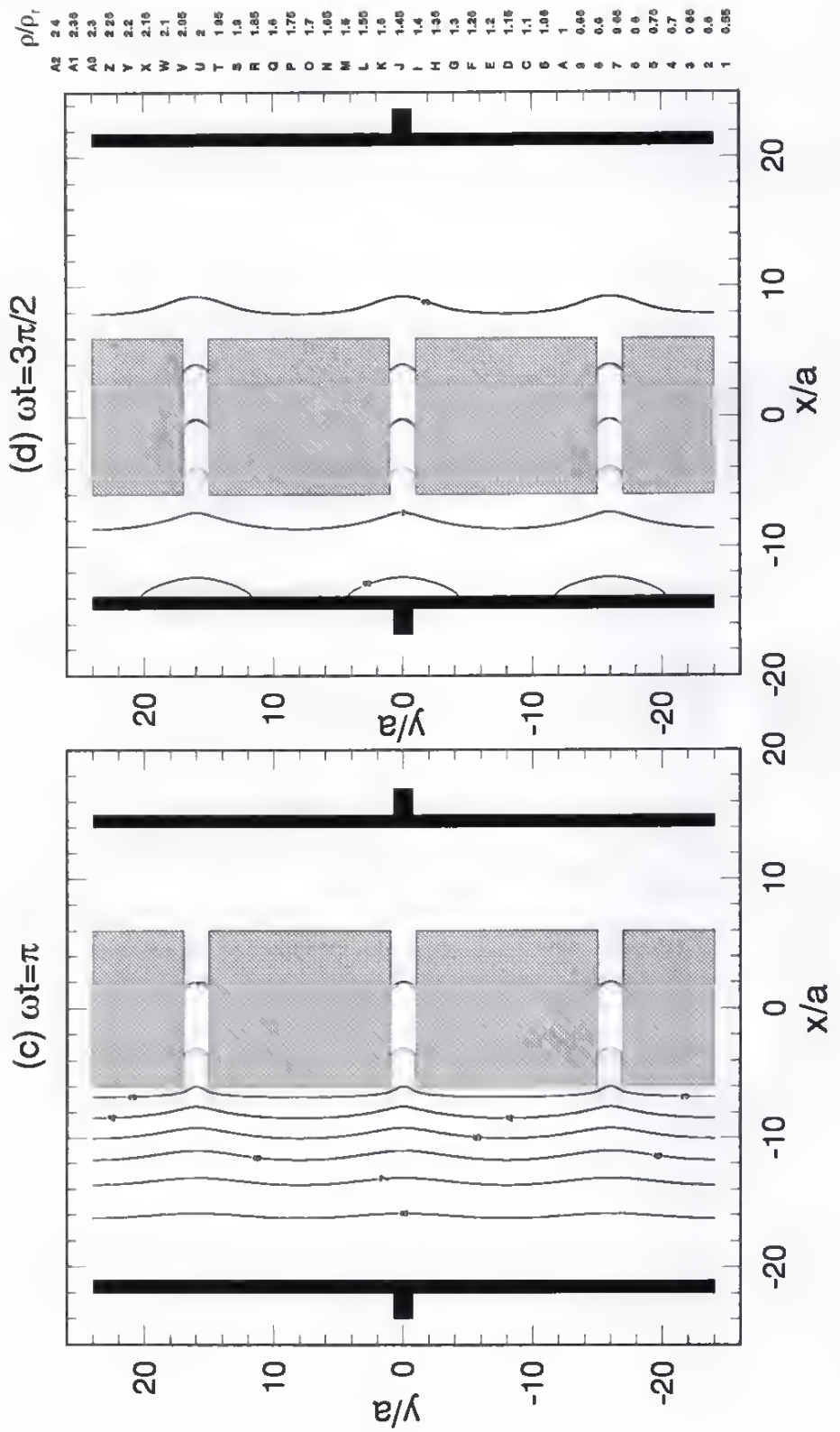

Fig. 4.6--continued

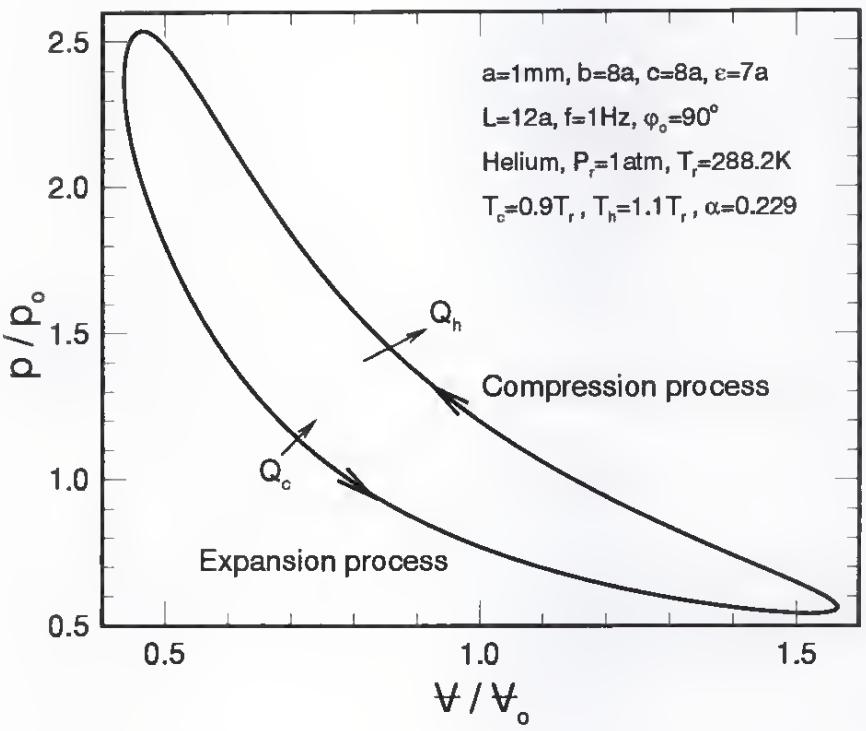

Fig. 4.7 P-V diagram of Case 1

input is P = 14.075D watts (as mentioned before, the symbol "D" represents the third dimension in meters). The rate at which the gas absorbs heat through the solid surfaces having cold temperature (T_c) is defined as the cooling capacity and is denoted by Q_c, while the rate at which heat is rejected from the gas through the solid surfaces having hot temperature (T_h) is defined as the heating rate and denoted by Q_h. Heat can also be conducted into or out of the channel walls along which the temperature distribution is linear. This is an undesirable leakage, the rate of which is denoted by Q_{leak}. The quantities here are: Q_c = 11.574D watts, Q_h = 21.643D watts, and Q_{leak} = 3.990D watts. So the total rate of energy into the system is

$$P + Q_c = 14.075D + 11.574D = 25.649D,$$

and the total rate of energy out of the system is

$$Q_h + Q_{leak} = 21.643D + 3.990D = 25.633D.$$

Hence the overall energy balance is excellent.

In the above discussions, the factor "D" and unit "watt" always go with the quantities: Q_c, Q_h, Q_{leak} and P. The factor and units will be omitted in the following for simplicity.

4.2 Model Comparison

To compare Models A1 and A2, consider Cases 2 and 3. As listed in Table 4.1, all the conditions for these cases are the same except that in Case 2 the temperature along the entire channel wall is linear, while in Case 3 the channel wall temperature is linear only along the middle segment of the channel and the wall temperature is constant along

either end segment. Table 4.2 compares the performances of the two cases. The negative value of Q_{leak} in Case 3 means that heat is added into the gas through the channel walls having a linear temperature distribution. In the table, COP stands for the coefficient of performance, which is defined as (Walker 1973)

Table 4.2 Comparison of Models A1 and A2

	Case 2 Model A1	Case 3 Model A2
Q_c	12.7403	11.8207
Q_h	17.4084	19.3578
Q_{leak}	2.4482	-0.3929
P	7.1340	7.1626
COP	1.7859	1.6503
η_r	39.69%	36.67%

$$\text{COP} = \text{Cooling capacity / Power input} = Q_c / P. \tag{4.2}$$

The COP of Case 2 is 1.7859, and that of Case 3 is 1.6503; the latter is only slightly lower than the former. According to the Carnot theorem, of all the thermodynamic cycles with common values for the maximum and minimum temperatures, pressures and volumes, the Carnot cycle has the maximum COP. For a cooling device, the COP of a Carnot cycle is (Walker 1973)

$$(\text{COP})_{\text{carnot}} = T_c / (T_h - T_c). \tag{4.3}$$

In Table 4.2, the symbol η_r represents the relative efficiency defined by (Walker 1973)

$$\eta_r = \text{Actual COP / Carnot COP} = \text{COP} / (\text{COP})_{\text{carnot}}. \tag{4.4}$$

The relative efficiency of an actual device usually varies between 40% and a few percent depending on the size of the device and the operation conditions. Here the relative efficiency of either Case 3 or 4 is only slightly below 40%. In terms of the cooling capacity, power input and hence COP, Models A1 and A2 have almost the same

performance under the given conditions.

Next compare Models A2 and B2. Case 3 uses the single-channel model A2 and Case 4 uses the multichannel model B2, with all other conditions being the same. It can be seen from Table 4.3 that Case 4 gives a cooling capacity of 11.3202, which is quite close to Case 3's 11.8207. Case 4 requires a power input of 11.3809, while Case 3 requires only 7.1626. As a result, Case 4 has a COP as low as 0.9947. The use of the multichannel model in Case 4 makes the compression and expansion processes closer to adiabatic than in Case 3 where single-channel model is used, so Case 4 should have a larger range of pressure variations despite the same volumetric changes for the two cases. Computed data (not tabulated here) indicate pressure limits of [0.64, 2.12] (atm) for Case 3 and limits of [0.57, 2.22] for Case 4. That explains why the latter case needs a larger power input than the former. The compression and expansion processes in Case 4 produce lower temperature in the left chamber and higher temperature in the right chamber, respectively, than in Case 3; the cooling or heating of Case 4, however, is still close to the counterpart of Case 3, because the heat exchanging area of Case 4 is much smaller than that of Case 3. Even though

Table 4.3 Comparison of Models A2 and B2

	Case 3 Model A2	Case 4 Model B2
Q_c	11.8207	11.3202
Q_h	19.3578	22.9956
Q_{leak}	-0.3929	-0.3421
P	7.1626	11.3809
COP	1.6503	0.9947
η_r	36.67%	22.10%

the multichannel model has a lower COP than the single-channel model does, the former is more practical from an engineering viewpoint.

4.3 Comparison of Using Helium and Air

The most widely used working gases for Stirling-type machines are air, helium and hydrogen. The selection of a gas for a specific Stirling cooling device not only depends on the thermodynamic performance of the gas, but also depends on other factors such as cost, availability, safety and so on (Reader and Hooper 1983). With the computer code, it is very convenient to compare the performances of working gases. Consider Cases 4 and 5, in which geometric parameters, temperature boundary conditions, piston oscillation frequencies and amplitudes are the same, but helium is the working gas in the former and air in the latter. From Table 4.4 it can be seen that helium produces a cooling capacity twice as large as air does, while the power input needed for one case is close to the other. As a result, helium is about twice as efficient as air under the given conditions.

Table 4.4 Comparison of helium and air

	Case 4 Helium	Case 5 Air
Q_c	11.3202	5.2169
Q_h	22.9956	14.1773
Q_{leak}	-0.3421	1.2477
P	11.3809	10.2219
COP	0.9947	0.5104
η_r	22.10%	11.34%

There are mainly two reasons contributing to this. First, the monatomic gas helium has a ratio of specific heats of 1.67, which is higher than air's 1.40. So, for the

same amount of expansion, more cooling is produced by helium than by air. Second, helium has a smaller Prandtl number than air (0.67 versus 0.72) and a kinematic viscosity eight times as large as air. As result, the channel's heat regeneration for helium is better than for air. And a detailed discussion on the regeneration will be found in Section 4.8.

4.4 Phase Angle Effect

In order to examine the effect of phase angle on the performances of the models, five runs (Cases 6 through 10 in Table 4.1) were made with phase angles of $\varphi_o = 45°$, 75°, 90°, 105° and 135°, respectively, with other parameters being maintained constant. Figure 4.8 plots the cooling capacity (Q_c), rate of heat rejected (Q_h), power input (P) and COP versus the phase angle φ_o. The figure shows that each of the four quantities takes its maximum in the range of phase angles covered, and that the phase angle corresponding to the maximum value of one quantity may differ from that of another. For instance, the power input has a maximum at $\varphi_o \simeq 110°$, the cooling capacity a maximum at $\varphi_o \simeq 96°$, and COP a maximum at $\varphi_o \simeq 75°$. The optimum phase angle for the cooling power is not optimum for COP. Generally speaking, the phase angles corresponding to the maxima are not too far off 90°, and each of the four quantities shown in the figure is not very sensitive to changes in φ_o near the optimum phase angle. These observations based on the numerical simulations are in agreement with experimental data (Reader and Hooper 1983, pp. 75-77).

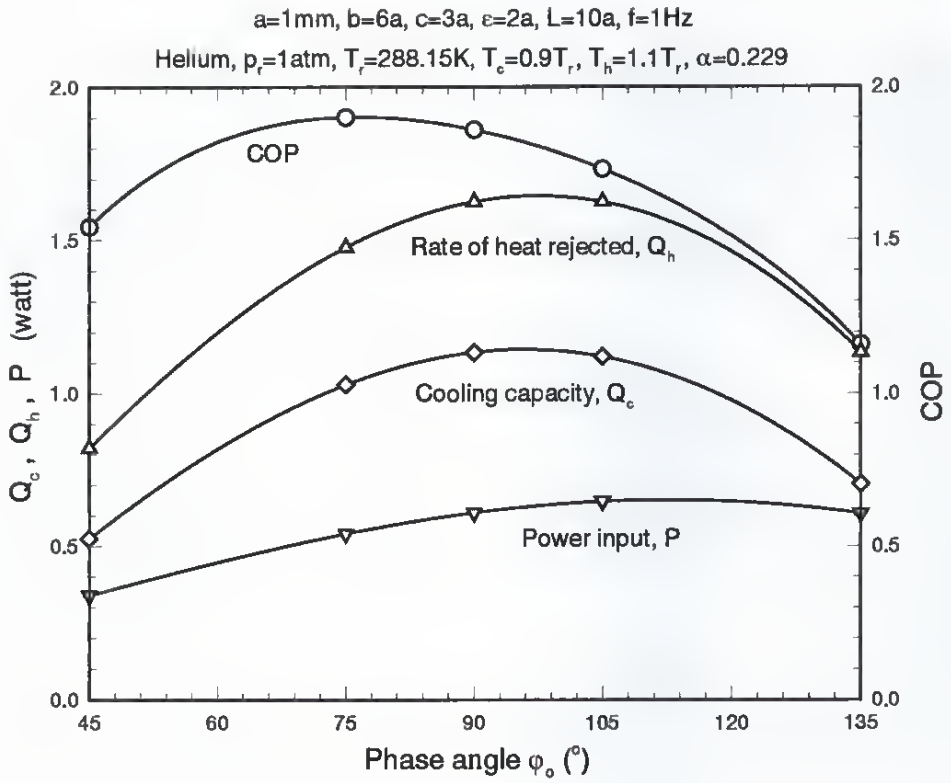

Fig. 4.8 Phase angle effects

4.5 Impact of Varying Refrigeration Temperatures on Performances

To understand the effects of changing the refrigeration temperature on the performances, several runs (Cases 2 and 11 through 15) were made, in which the temperature difference between the cold and hot chambers was changed to a large extent while all other parameters were kept unchanged. In Fig. 4.9, the cooling capacity, power input and COP are plotted versus the ratio of the cold to hot-end temperature, T_c/T_h. Also plotted in the figure is the mean rate at which heat is conducted and convected into the cold chamber through the gas at the cross section of the channel exit. This rate is regarded as a loss (denoted by Q_{loss}), because it will consume some cooling

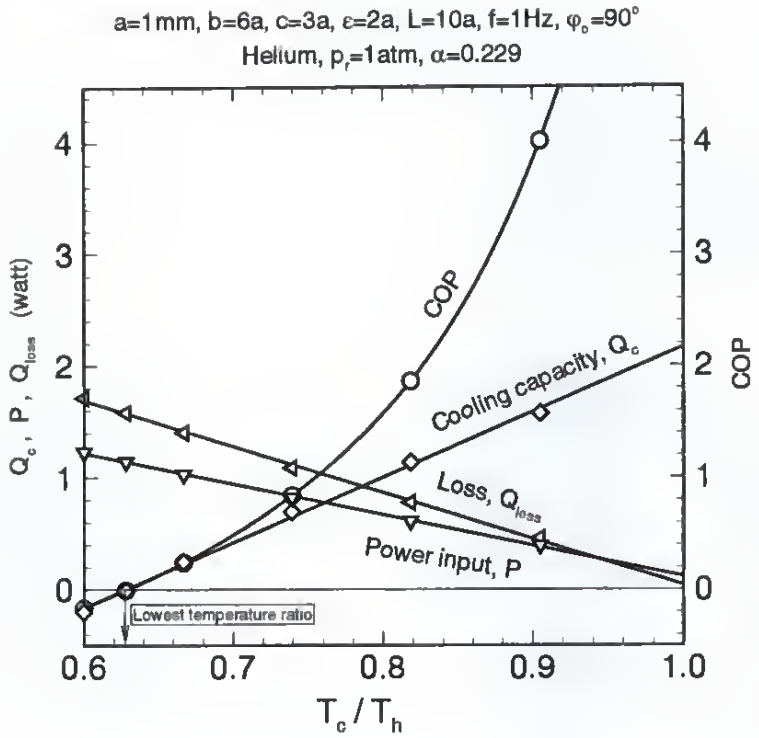

Fig. 4.9 Refrigeration temperature effects

made by expansion.

The cooling capacity, power input, the loss and the COP all vary monotonously with the temperature ratio. When the refrigeration temperature rises, the cooling capacity increases, but the power input and the loss decrease, therefore the COP increases, too. The closer the cold chamber temperature is to the hot-end temperature (usually the ambient), the better is the performance. For instance, when T_c/T_h equals 0.76, the COP is about 1. However, as T_c/T_h is increased to 0.9, the COP is close to 4. Such phenomena were also reported by McDonald and coworkers (McDonald et al. 1994) based on their design analysis and experimental data with an actual Stirling refrigerator.

When the cold chamber wall temperature is set too low, cooling is no longer possible. Instead, heat is rejected out of the gas in the left chamber through the walls. That is indicted by the negative cooling capacity in the figure. If the hot-end temperature T_h is 300 K, the lowest obtainable refrigeration temperature will be about 189 K under the operation conditions considered. The large heat loss at low refrigeration temperatures can consume all the cooling produced by expansions.

4.6 Changing Channel Length

Increasing the channel length (or the regenerator length) will decrease the temperature gradient along the channel, and therefore can reduce the conduction loss. Comparing Case 2 and Case 16 (Table 4.5) will demonstrate that. The channel length in the former is 24a and that in the latter is 12a, and other parameters in both cases are the same. The loss with the longer channel is 0.6131, which is less than 1.2443--the counterpart with the shorter channel. However, the cooling capacity with the longer channel is 12.7403, which is surprisingly even less than the value (13.745) of the cooling capacity with the shorter channel. The reason for this is that although the loss is reduced by lengthening the channel, meanwhile the volume that cannot be swept by the pistons--the

Table 4.5 Comparison of cases with different channel lengths

	Case 2 L=24a	Case 16 L=12a
Q_{loss}	0.6131	1.2443
Q_c	12.7403	13.7450
P	7.1340	8.6155
COP	1.7859	1.6000

dead volume--is also increased, therefore the cooling produced by expansion decreases. The net effect (i.e., the available cooling Q_c) depends on these two competing factors under specific operation conditions. Despite such complexity, it is always true that increasing the channel length also increases the COP because the loss is reduced. Table 4.5 does show that the COP with the longer channel is 1.7859 but that with the shorter one is only 1.6.

4.7 Effects of Changing the Ratio of Chamber Width to Channel Width

Under given conditions, if the ratio of chamber width (2b) to channel width (2a), i.e. b/a, is too small, the gas in the cold chamber is not effectively separated from that in the hot; besides, the effective cooling surface is also too small. On the other hand, if the ratio is too large, the gas in one chamber cannot be promptly transferred to the other when needed. Either situation may degrade the cooling performance. For the multichannel models, in addition to the COP, another appropriate measure of the performance is the cooling capacity per unit area of the chamber cross section, i.e. Q_c /(2bD), which indicates how economically the device uses space. Four cases were run with the following values of b/a: 4 (Case 18), 8 (Case 1), 12 (Case 18) and 15 (Case 19). Figure 4.10 plots COP and Q_c /(2bD) versus b/a. The figure shows that both COP and Q_c /(2bD) vary with b/a, and there exists an optimum value of b/a for either quantity. When b/a is approximately 6.4, the efficiency of performance takes its maximum value of about 0.84. When b/a is about 11.5, the quantity Q_c /(2bD) reaches a maximum value of about 750 Watts/m^2.

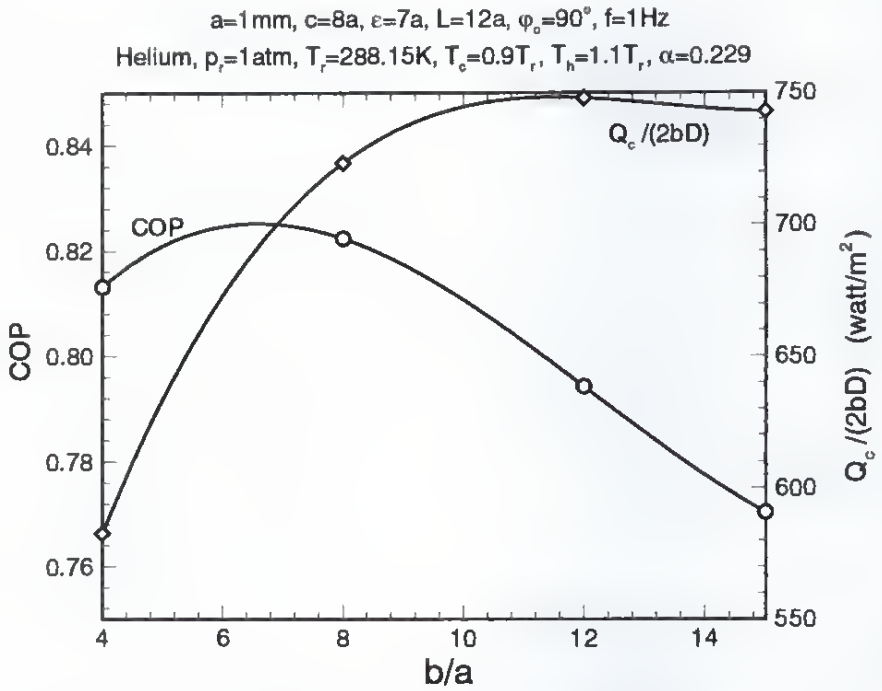

Fig. 4.10 Effects of changing the ratio of chamber width to channel width

4.8 Discussion on Regeneration

It is known that the regeneration efficiency can greatly affect the performances of a Stirling device. This section discusses the condition required for the channel with a linear temperature distribution to provide adequate regeneration. For good regeneration, there should be enough time for the gas flowing through the channel to adjust its temperature to the that of the local channel wall. The time scale of the thermal diffusion across the channel is

$$t_{dif} = \frac{a^2}{\kappa} = \frac{a^2 Pr}{\nu} , \tag{4.5}$$

where κ is the thermal diffusivity. The residence time during which the gas passes through the channel and exchanges heat with the channel is

$$t_{res} = \frac{L}{U_m} , \tag{4.6}$$

in which U_m is the mean magnitude of the gas velocity within the channel. This quantity is estimated by using the ratio of the chamber width (2b) to the channel width (2a) and the mean magnitude of the piston velocity U_{pm}. Since the piston velocity is in the form of $\varepsilon\omega\cos(\omega t+\varphi)$, the quantity U_{pm} is $\varepsilon\omega/\sqrt{2}$. Then one has

$$U_m = \frac{b}{a} U_{pm} = \frac{b}{a} \frac{\varepsilon \omega}{\sqrt{2}}. \tag{4.7}$$

It is necessary for t_{res} to be greater than t_{dif}, i.e.,

$$t_{res} > t_{dif} . \tag{4.8}$$

Substituting Eqs. (4.5)-(4.7) into Eq. (4.8) and then rearranging terms yield

$$\beta = \frac{1}{\sqrt{2}} \frac{b}{a} \frac{\varepsilon}{L} \alpha^2 Pr < 1 . \tag{4.9}$$

The dimensionless parameter β defined in Eq. (4.9) is a combination of two other parameters related to the geometry (i.e. b/a and ε/L), flow oscillation (i.e. α) and heat transfer (i.e. Pr). For effective regeneration, β should be kept far below unity.

Compare Cases 8 and 20. The parameter β in the former is 0.0298, and that in the latter is 0.298. Such an increase in β is made possible by increasing the oscillation

frequency by nine times. Figures 4.11 (a) and (b) plot the temperature distributions along the x axis at eight time instants for the two cases respectively. For the case with the smaller β, at all the time instants and within almost the entire channel, the gas temperature is always very close to the local channel wall temperature. This indicates that the channel functions well as a regenerator. However, for the case with the larger β, the temperature of the gas within the channel deviates significantly from that of the local wall. As a result, the case with β=0.0298 has a COP of 1.8606, but the case with β=0.298 has merely a COP of 0.9265. The comparison made here clearly shows the role played by the parameter β and the need to keep this well below unity in a typical channel regenerator.

(a)

a=1mm, b=6a, c=3a, ε=2a, L=10a, φ_o=90°, f=1Hz, α=0.229
Helium, p_r=1atm, T_r=288.15K, T_c=0.9T_r, T_h=1.1T_r

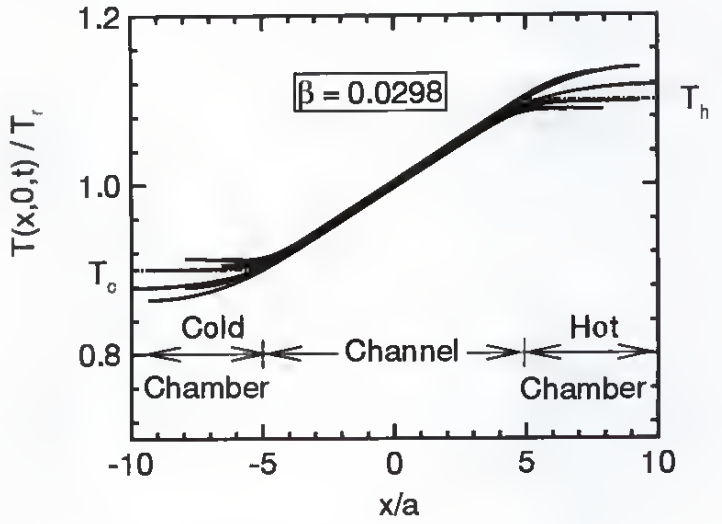

a=1mm, b=6a, c=3a, ε=2a, L=10a, φ_o=90°, f=10Hz, α=0.724

(b) Helium, p_r=1atm, T_r=288.15K, T_c=0.9T_r, T_h=1.1T_r

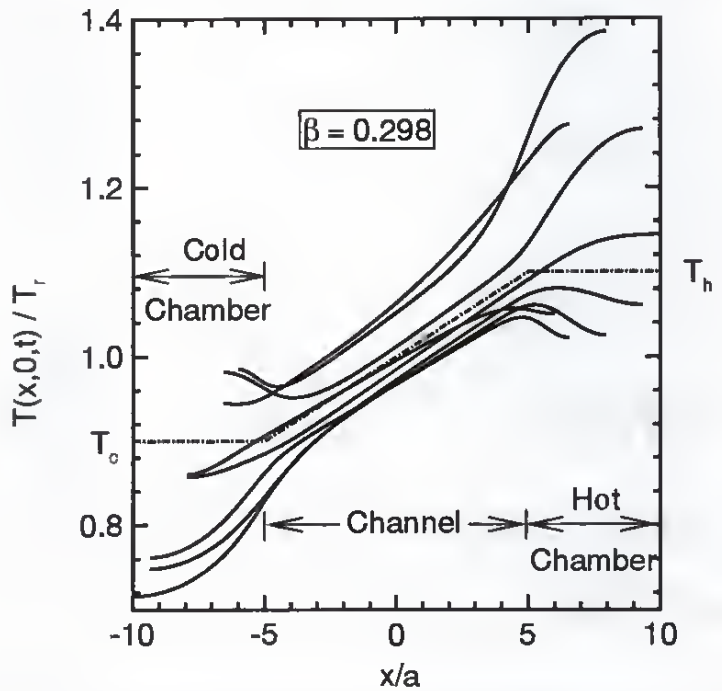

Fig. 4.11 Temperature distributions along x axis for two different β's (a) β = 0.0298; (b) β = 0.298.

CHAPTER 5
CONCLUDING REMARKS

A numerical technique was devised to separate the hydrodynamic and thermodynamic pressures for low-Mach number variable-density flows with heat transfer, which occur in reciprocating thermodynamic machines. Separation of these two pressures different in orders of magnitudes avoids the catastrophic cancellations in numerically evaluating the pressure gradients, and so the technique can increase computational accuracy and efficiency substantially (potential saving on CPU time is about 30% and that on storage and memory is 50%). It can be easily incorporated to any existing pressure-based numerical algorithms.

Two-dimensional models of three-component Stirling microrefrigerators were developed in this study. The models consist of all three heat exchangers: heater, cooler and regenerator. The heater and cooler are ended with pistons oscillating out of phase, and connected by narrow channels with a linear wall-temperature distribution, simulating the regenerator. Numerical computations were made for the time-periodic, variable-density flow and heat transfer within domains with moving boundaries by using the SIMPLE algorithm incorporated with a moving grid technique and with the newly devised pressure-splitting method. Such a solution methodology was proven to be feasible--accurate and efficient--for the complex flow and heat transfer problems in the

Stirling-type devices. This is the first reported attempt to systematically discuss the numerical aspects pertaining to the simulations of Stirling devices. Results based on the microrefrigerator models agreed very well with the experimental data obtained from actual devices.

The model's regeneration and cooling performance are sensitive to the dimensionless parameter that is the product of Womersley number squared, Prandtl number, the relative piston strokes, and the ratio of chamber width to channel width. This parameter should be kept far below unity for the connecting channels to function well as a regenerator.

As the cold chamber wall temperature decreases, the cooling capacity decreases linearly, but the power input increases linearly, and consequently the performance degrades. For a set of given operation conditions, there is a lowest temperature below which no cooling is possible. This is caused by the increasing cooling loss through the channel as the cold chamber temperature decreases. Lengthening the channels decreases such loss, but meanwhile increases the dead space, which in turn reduces the cooling made by the expansion. The net effect depends on these two competing factors under specific conditions.

The phase angle affects the cooling capacity and efficiency. The phase angle that results in the maximum cooling capacity may not necessarily result in the maximum efficiency. The optimum phase angle for either cooling capacity or efficiency is near 90°.

The ratio of the chamber width to the channel width also affects the cooling

performance. Under given operation conditions, there is an optimum ratio for the cooling capacity and efficiency respectively.

Future work on this topic should be in the following directions. First, turbulence models for oscillatory internal flows should be incorporated into the computations so that simulations can also be made for larger devices and for higher frequencies. Second, model the regenerator as porous medium to simulate the conjugate heat transfer more accurately. Third, use a five-component model instead of the three-component model. Finally, the dimensions of the model should be increased from two to three. These extensions will need a very large increase in computing resources of both computer memory and CPU time, and it will be necessary to use parallel computations on Cray supercomputers.

REFERENCES

Ahn, K.H. and Ibrahim, M.B., "A 2-D Oscillating Flow Analysis in Stirling Engine Heat Exchanger," NASA TM 103781, ICOMP-91-04, 1991.

Andraka, C.E., Goods, S.H., Bradshaw, R.W., Moreno, J.B., Moss T.A. and Jones S.A., "NAK Pool-Boiler Bench-Scale Receiver Durability Test: Test Results and Materials Ananysis," Proceedings of the 29th Intersociety Energy Conversion Engineering Conference, AIAA, 1994, Vol. 4, pp. 1942-1949.

Beam, R.M. and Warming, R.F., "An Implicit Factored Scheme for the Compressible Navier-Stokes Equations," AIAA Journal, Vol. 16, No. 4, 1978, pp. 393-402.

Berchowitz, D.M., "Free-Piston Stirling Coolers for Intermediate Lift Temperatures," Proceedings of the 27th Intersociety Energy Conversion Engineering Conference, SAE, 1992, Vol.5, pp. 115-121.

Cairelli, J.E., Geng, S.M. and Skupinski, R.C., "Results From Basline Tests of the SPRE I and Comparison with Code Model Predications," Proceedings of the 24th Intersociety Energy Conversion Engineering Conference, IEEE, 1989, Vol.5, pp. 2249-2256.

Cairelli, J.E., Geng, S.M., Wong, W.A., Swec, D.M., Doeberling, T.J., Madi, F.J. and Vora, D.C., "1993 Update on Results of SPRE Testing at NASA Lewis," Proceedings of the 28th Intersociety Energy Conversion Engineering Conference, ACS, 1993, Vol.2, pp. 633-638.

Cairelli, J.E., Swec, D.M. and Skupinski, R.C. and Rauch, S., "Update on Results of SPRE Testing at NASA," Proceedings of the 25th Intersociety Energy Conversion Engineering Conference, AIChE, 1990, Vol.5, pp. 237-244.

Cairelli, J.E., Swec, D.M., Wong, W.A., Doeberling, T.J. and Madi, F.J., "Update on Results of SPRE Testing at NASA Lewis," Proceedings of the 26th Intersociety Energy Conversion Engineering Conference, ANS, 1991, Vol.5, pp. 217-222.

Chan, C.K., Tward, E. and Burt, W.W., "Overview of Cryocooler Technologies for Space-Based Electronics and Sensors," in Advances in Cryogenic Engineering, Vol. 35 (Editor: R.W. Fast), Plenum Press, New York, 1990, pp. 1239-1250.

Chase, V., "Here's a Chilling Thought: How to Keep Cool Without CFCs," R&D Magazine, Vol. 37, No. 10, 1995, pp. 39-40.

Demirdžić, I. and Perić, M., "Finite Volume Method for Prediction of Fluid Flow in Arbitrarily Shaped Domains with Moving Boundaries," International Journal for Numerical Methods in Fluids, Vol. 10, 1990, pp. 771-790.

Diver, R.B., Andraka, C.E., Moreno, J.B., Adkins, D.R., and Moss, T.A., "Trends in Dish-Stirling Receiver Designs," Proceedings of the 25th Intersociety Energy Conversion Engineering Conference, AIChE, 1990, Vol.5, pp. 303-310.

Dochat, G. "Free-Piston Space Stirling Technology Program: An Update," Proceedings of the 25th Intersociety Energy Conversion Engineering Conference, AIChE, 1990, Vol.5, pp. 219-233.

Dochat, G. and Dhar, M., "Free-Piston Stirling Component Test Power Converter," Proceedings of the 26th Intersociety Energy Conversion Engineering Conference, ANS, 1991, Vol.5, pp. 239-244.

Fox, R.W. and McDonald, A.T., Introduction to Fluid Mechanics, Second Edition, John Wiley & Sons, New York, 1978, pp. 307-308.

Gedeon, D., "Manifest: A Computer Program for 2-D Flow Modeling in Stirling Machines," NASA Contractor Report 182290, 1989.

Geng, S.M. and Tew, R.C., "Comparisons of GLIMPS and HFAST Stirling Engine Code Predictions with Experimental Data," Proceedings of the 27th Intersociety Energy Conversion Engineering Conference, SAE, 1992, Vol.5, pp. 53-58.

Golub, G.H. and Ortega, J.M., Scientific Computing and Differential Equations: An Introduction to Numerical Methods, Academic Press, San Diego, CA, 1992, pp. 6-8.

Hansen, A.G., Fluid Mechanics, Wiley, New York, 1967.

Hirsch, C., Numerical Computation of Internal and External Flows, John Wiley & Sons, New York, 1988, Vol. 1, pp. 474-476.

Hornbeck, R.W., Numerical Methods, Prentice-Hall, Englewood Cliffs, NJ, 1982, pp. 66-89.

Huang, S.C., "HFAST--A Harmonic Analysis Program for Stirling Cycles," Proceedings of the 27th Intersociety Energy Conversion Engineering Conference, SAE, 1992, Vol.5, pp. 47-52.

Ibrahim, M., Hashim,W. Tew, R.C. and Dudenhoefer, J.E., "Heat Transfer in Oscillating Flows with Sudden Change in Cross Section," Proceedings of the 27th Intersociety Energy Conversion Engineering Conference, SAE, 1992, Vol. 5, pp. 503-508.

Ibrahim, M., Kannapareddy, M., Tew, R.C. and Dudenhoefer, J.E., "Instantaneous Heat Transfer Coefficient Based upon Two-Dimensional Analysis of Stirling Space Engine Components," Proceedings of the 26th Intersociety Energy Conversion Engineering Conference, ANS, 1991, Vol. 6, pp. 149-159.

Isshiki, N., Kohira, Y., Sato, N. and Kinoshita, H., "Experimental Studies on Alpha Type Stirling Cooler," Proceedings of the 29th Intersociety Energy Conversion Engineering Conference, AIAA, 1994, Vol. 4, pp. 1813-1816.

Isshiki, N., Watanabe, H., Shishido, K. and Watanabe, K., " R&D on Small Solar Stirling Engines TNT-2 & 3, NAS-1," Proceedings of the 26th Intersociety Energy Conversion Engineering Conference, ANS, 1991, Vol.5, pp. 382-387.

Jones, D. "Free-Piston Stirling Engine Scaling Study," Proceedings of the 25th Intersociety Energy Conversion Engineering Conference, AIChE, 1990, Vol.5, pp. 245-249.

Karki, K.C., "A Calculation Procedure for Viscous Flows at All Speeds in Complex Geometries," Ph.D. Thesis, University of Minnesota, June 1986, pp. 39-45.

Keck, T., Schiel, W. and Benz, R., "An Innovative Dish/Stirling System," Proceedings of the 25th Intersociety Energy Conversion Engineering Conference, AIChE, 1990, Vol.6, pp. 317-322.

Kim, S.-T., Cho, K.-S. and Chung W.-S., "Study of Stirling Cycle Refrigerator," Proceedings of the 28th Intersociety Energy Conversion Engineering Conference, ACS, 1993, Vol.2, pp. 615-619.

Köhler, J.W.L., "The Gas Refrigerating Machine and Its Position in Cryogenic Technique," in Progress in Cryogenics, Vol.2 (Editor: K. Mendelssohn), Academic Press, New York, 1960, pp. 41-67.

Kormhauser, A.A. and Smith, J.L. Jr., "Heat Transfer with Oscillating Pressure and Oscillating Flow," Proceedings of the 24th Intersociety Energy Conversion Engineering Conference, IEEE, 1989, Vol. 5, pp. 2347-2353.

Kurzweg, U.H. and Zhao, A.X., "The Stirling Micro-refrigerator: An Innovative Cooling Device for Space Applications," ISRP 92-93 Final Report-Subcontract No. NGT40015, 1993.

Loktionov, Y.V., "Conceptual Design of Free-Piston Stirling Conversion System for Solar Power Units," Proceedings of the 26th Intersociety Energy Conversion Engineering Conference, ANS, 1991, Vol.5, pp. 370-375.

McDonald, K., Berchowitz, D., Rosenfeld, J. and Lindemuth, J. "Stirling Refrigerator for Space Shuttle Experiments," Proceedings of the 29th Intersociety Energy Conversion Engineering Conference, AIAA, 1994, Vol. 4, pp. 1807-1812.

Nambudripad, N. "Small refrigerators," in Cryogenic Engineering (Editor: B.A. Hands), Academic Press, London, 1986, pp. 431-455.

Organ, A.J., Thermodynamics and Gas Dynamics of the Stirling Cycle Machine, Cambridge University Press, 1992.

Otaka, T., Saito, K., Saito, T., Araoka, K. and Kagawa, N., "Study on a 100W-Class Stirling Cycle Cooler--Experimental results of Operating Characteristics," Proceedings of the 28th Intersociety Energy Conversion Engineering Conference, ACS, 1993, Vol.2, pp. 621-626.

Patankar, S.V., Numerical Heat Transfer and Fluid Flow, Hemisphere, Washington, D.C., 1980.

Reader, G.T. and Hooper, C., Stirling Engines, E. & F. N. Spon, New York, 1983.

Shaltens, R.K. and Schreiber, J.G., "Comparison of Conceptual Designs for 24 kWe Advanced Stirling Conversion Systems for Dish Electric Applications," Proceedings of the 24th Intersociety Energy Conversion Engineering Conference, IEEE, 1989, Vol. 5, pp. 2305-2315.

Sherman, A. "History, Status and Future Applications of Spaceborne Cryogenic Systems," in Advances in Cryogenic Engineering, Vol. 27 (Editor: R. W. Fast), Plenum Press, New York, 1982, pp. 1007-1029.

Shimko, M.A., Wallis, P.N. and Martin, C.M., "Diaphragm Defined Stirling Refrigerator," Proceedings of the 29th Intersociety Energy Conversion Engineering Conference, AIAA, 1994, Vol. 4, pp. 1796-1801.

Shyy, W., Computational Modeling for Fluid Flow and Interfacial Transport, Elsevier, Amsterdam, the Netherlands, 1994, pp. 156-163.

Smith, J.L. Jr., Lienhard, J.H. V, Tziranis, A.K. and Ho, Yung, "M.I.T. Stirling-Cycle Heat Transfer Apparatus," Proceedings of the 27th Intersociety Energy Conversion Engineering Conference, SAE, 1992, Vol. 5, pp. 509-516.

Tang, X. and Cheng, P., "Correlations of the Cycle-Averaged Nusselt Number in a Periodically Reversing Pipe Flow," Int. Comm. Heat Mass Transfer, Vol. 20, No. 2, 1993, pp. 161-172.

Tew, R.C., "Overview of Heat Transfer and Fluid Flow Problem Areas Encountered in Stirling Engine Modeling," in Fluid Flow and Heat Transfer in Reciprocating Machinery (Editors: T. Morel, J.E. Dudenhoefer, T. Uzkan and P.J. Singh), ASME, New York, 1987, pp. 77-88.

Tew, R.C., "Status of Several Stirling Loss Characterization Efforts ans Their Significance for Stirling Space Power Development," Proceedings of the 23rd Intersociety Energy Conversion Engineering Conference, ASME, 1988, Vol.1, pp. 113-119.

Tew, R.C. and Geng, S.M., "Overview of NASA Supported Stirling Thermodynamic Loss Research," Proceedings of the 27th Intersociety Energy Conversion Engineering Conference, SAE, 1992, Vol.5, pp. 489-494.

Thieme, L.G. and Swec, D.M., "Overview of the NASA Lewis Component Technology Program for Stirling Program for Stirling Power Converters," Proceedings of the 27th Intersociety Energy Conversion Engineering Conference, SAE, 1992, Vol.5, pp. 283-288.

Thompson, J.F., Warsi, Z.U.A. and Mastin, C.W., Numerical Grid Generation: Foundations and Applications, North-Holland, 1985, pp. 307-308.

Timmerhaus, K.D. and Flynn, T.M., Cryogenic Process Engineering, Plenum Press, New York, 1989.

Walker, G., Stirling-Cycle Machines, Oxford University Press, London, 1973.

Walker, G., Fauvel, O.R., Reader, G., Ellison, W., Zylstra, S. and Scott, M.J., "Commercial Applications for Stirling Refrigerators," Proceedings of the 23rd Intersociety Energy Conversion Engineering Conference, ASME, 1988, Vol.1, pp. 15-19.

Walker, G., Reader, G., Fauvel, R. and Bingham, E.R., "Stirling, Near-Ambient Tempetrature Refrigerators: Innovative Compact Designs," Proceedings of the 27th Intersociety Energy Conversion Engineering Conference, SAE, 1992, Vol.5, pp. 93-96.

West, C.D., Principles and Applications of Stirling Engines, Van Nostrand Reinhold, New York, 1986.

White, M.A., "Implantable Energy Source for Artificial Hearts," Proceedings of the 1st International Symposium on Current Problems for Future Development of Artificial Heart and Assis Device," Springer-Verlag, 1985, pp. 36-48.

Wong, W.A., Cairelli, J.E., Swec, D.M., Doeberling T.J., Lakatos, T.F. and Madi, F.J., "NASA Lewis Stirling Testing and Analysis with Reduced Number of Cooler Tubers," Proceedings of the 27th Intersociety Energy Conversion Engineering Conference, SAE, 1992, Vol.5, pp. 443-448.

BIOGRAPHICAL SKETCH

Guobao Guo was born on January 17, 1963 in Nanyang County, Henan Province, the People's Republic of China. In 1980, he enrolled in the Aerospace Engineering Department of the Northwestern Polytechnical University, Xi'an, Shaanxi Province, P.R. China. He received his bachelor's degree in 1984 and master's in 1987, and then he continued his study as a Ph.D. candidate at that university till 1989. In that year he came to the United States and enrolled as a graduate student in the Department of Aerospace Engineering, Mechanics and Engineering Science of the University of Florida.

I certify that I have read this study and that in my opinion it conforms to acceptable standards of scholarly presentation and is fully adequate, in scope and quality, as a dissertation for the degree of Doctor of Philosophy.

Ulrich H. Kurzweg, Chairperson
Professor of Aerospace Engineering,
Mechanics and Engineering Science

I certify that I have read this study and that in my opinion it conforms to acceptable standards of scholarly presentation and is fully adequate, in scope and quality, as a dissertation for the degree of Doctor of Philosophy.

Chen-Chi Hsu
Professor of Aerospace Engineering,
Mechanics and Engineering Science

I certify that I have read this study and that in my opinion it conforms to acceptable standards of scholarly presentation and is fully adequate, in scope and quality, as a dissertation for the degree of Doctor of Philosophy.

Wei Shyy
Professor of Aerospace Engineering,
Mechanics and Engineering Science

I certify that I have read this study and that in my opinion it conforms to acceptable standards of scholarly presentation and is fully adequate, in scope and quality, as a dissertation for the degree of Doctor of Philosophy.

David W. Mikolaitis
Associate Professor of Aerospace Engineering, Mechanics and Engineering Science

I certify that I have read this study and that in my opinion it conforms to acceptable standards of scholarly presentation and is fully adequate, in scope and quality, as a dissertation for the degree of Doctor of Philosophy.

Kermit N. Sigmon
Associate Professor of Mathematics

This dissertation was submitted to the Graduate Faculty of the College of Engineering and to the Graduate School and was accepted as partial fulfillment of the requirements for the degree of Doctor of Philosophy.

May 1996

Winfred M. Phillips
Dean, College of Engineering

Karen A. Holbrook
Dean, Graduate School

LD
1780
1996
.G976l